

LOW FREQUENCY RAMAN SCATTERING IN AMORPHOUS
MATERIALS:

Fused quartz, "Pyrex" boro-silicate glass and Soda-lime silicate glass

by

Khaled Elozi, B.Sc. (Hons)

A thesis

submitted to the Department of physics

in partial fulfilment of the requirements

for the degree of

Master of Science

September 1991

Brock university

St. Catharines, Ontario

© Khaled Elozi, 1991

ACKNOWLEDGEMENT

I would like to express my thanks to my supervisor Dr. C. A. Plint for suggesting this problem and for his constant guidance throughout the course of this work. I would also like to thank my family, especially my mother and my uncle Dr. A. T. Shiglila, for their moral support. I also would like to acknowledge the financial support received from the libyan people during my stay at Brock. Also special thanks to Dr. R. C. Shukla for his help.

ABSTRACT

Raman scattering in the region 20 to 100 cm^{-1} for fused quartz, “pyrex” boro-silicate glass, and soft soda-lime silicate glass was investigated. The Raman spectra for the fused quartz and the pyrex glass were obtained at room temperature using the 488 nm exciting line of a Coherent Radiation argon-ion laser at powers up to 550 mW. For the soft soda-lime glass the 514.5 nm exciting line at powers up to 660 mW was used because of a weak fluorescence which masked the Stokes Raman spectrum. In addition it is demonstrated that the low-frequency Raman coupling constant can be described by a model proposed by Martin and Brenig (MB). By fitting the predicted spectra based on the model with a Gaussian, Poisson, and Lorentzian forms of the correlation function, the structural correlation radius (SCR) was determined for each glass. It was found that to achieve the best possible fit from each of the three correlation functions a value of the SCR between 0.80 and 0.90 nm was required for both quartz and pyrex glass but for the soft soda-lime silicate glass the required value of the SCR was between 0.50 and 0.60 nm. Our results support the claim of Malinovsky and Sokolov (1986) that the MB model based on a Poisson correlation function provides a universal fit to the experimental VH (vertical and horizontal polarizations) spectrum for any glass regardless of its chemical composition. The only deficiency of the MB model is its failure to fit the experimental depolarization spectra.

TABLE OF CONTENTS

	Page
List of figures.....	iv
1- Introduction.....	1
2- Theory.....	6
3- Experimental methods.....	16
4- Results.....	19
i) "Pyrex" boro-silicate glass.....	19
ii) Fused quartz.....	37
iii) Soft soda-lime silicate glass.....	52
5- Discussion.....	66
i) VV spectra.....	66
ii) VH spectra.....	69
iii) Depolarization spectra.....	71
6- Conclusion.....	76
Appendix I.....	79
References.....	81

LIST OF FIGURES

	Page
Fig. 1.1 Radial distribution function vs radius.....5 for a glass, crystal and dilute gas.	5
Fig. 1.2 Radial distribution function vs radius.....5 for amorphous quartz.	5
Figures for “pyrex” boro-silicate glass:	
Fig. 4.1 Experimental VV and VH Intensities vs Raman shift.....24	24
Fig. 4.2 VV anti-Stokes intensity vs Raman shift.....25	25
Fig. 4.3 Predicted and experimental VV anti-Stokes intensity vs Raman shift.....26	26
Fig. 4.4 Reduced intensity vs Raman shift..... 27	27
Fig. 4.5 Experimental and Gaussian predicted VH reduced spectrum vs Raman shift.....28	28
Fig. 4.6 Experimental and Gaussian predicted VV reduced spectrum vs Raman shift.....29	29
Fig. 4.7 Experimental and Gaussian predicted depolarization spectrum vs Raman shift.....30	30
Fig. 4.8 Experimental and Poisson predicted VH reduced spectrum vs Raman shift.....31	31
Fig. 4.9 Experimental and Poisson predicted VV reduced spectrum vs Raman shift.....32	32
Fig. 4.10 Experimental and Poisson predicted depolarization spectrum vs Raman shift.....33	33
Fig. 4.11 Experimental and Lorentzian predicted VH reduced spectrum vs Raman shift.....34	34
Fig. 4.12 Experimental and Lorentzian predicted VV reduced spectrum vs Raman shift..... 35	35
Fig. 4.13 Experimental and Lorentzian predicted depolarization spectrum vs Raman shift..... ..36	36

Figures for fused quartz:

	Page
Fig. 4.14 Experimental VV and VH Intensities vs Raman shift.....	41
Fig. 4.15 Reduced intensity vs Raman shift.....	42
Fig. 4.16 Experimental and Gaussian predicted VH reduced spectrum vs Raman shift.....	43
Fig. 4.17 Experimental and Gaussian predicted VV reduced spectrum vs Raman shift.....	44
Fig. 4.18 Experimental and Gaussian predicted depolarization spectrum vs Raman shift.....	45
Fig. 4.19 Experimental and Poisson predicted VH reduced spectrum vs Raman shift.....	46
Fig. 4.20 Experimental and Poisson predicted VV reduced spectrum vs Raman shift.....	47
Fig. 4.21 Experimental and Poisson predicted depolarization spectrum vs Raman shift.....	48
Fig. 4.22 Experimental and Lorentzian predicted VH reduced spectrum vs Raman shift.....	49
Fig. 4.23 Experimental and Lorentzian predicted VV reduced spectrum vs Raman shift.....	50
Fig. 4.24 Experimental and Lorentzian predicted depolarization spectrum vs Raman shift.....	51

Figures for soft soda-lime soft glass:

Fig. 4.25 Experimental VV and VH Intensities vs Raman shift.....	55
Fig. 4.26 Reduced intensity vs Raman shift.....	56
Fig. 4.27 Experimental and Gaussian predicted VH reduced spectrum vs Raman shift.....	57
Fig. 4.28 Experimental and Gaussian predicted VV reduced spectrum vs Raman shift.....	58
Fig. 4.29 Experimental and Gaussian predicted depolarization spectrum vs Raman shift.....	59

	Page
Fig. 4.30 Experimental and Poisson predicted VH reduced spectrum vs Raman shift.....	60
Fig. 4.31 Experimental and Poisson predicted VV reduced spectrum vs Raman shift.....	61
Fig. 4.32 Experimental and Poisson predicted depolarization spectrum vs Raman shift.....	62
Fig. 4.33 Experimental and Lorentzian predicted VH reduced spectrum vs Raman shift.....	63
Fig. 4.34 Experimental and Lorentzian predicted VV reduced spectrum vs Raman shift.....	64
Fig. 4.35 Experimental and Lorentzian predicted depolarization spectrum vs Raman shift.....	65

1- INTRODUCTION

A crystalline material is a solid consisting either of a single crystal or of many small crystals fused together. The regularity of shape and the symmetry of an individual crystal are the results of the regularity and symmetry of the arrangement of the atoms or molecules. The ordered arrangement extends over distances that are very large in comparison with the separation of near neighbour molecules. In an amorphous material the long range ordering, characteristic of the crystal, is absent although there is a degree of short range order that may extend out to three or four bond lengths for the component atoms.

The degree of order in a material can be characterised by the radial distribution function (RDF) which is proportional to the mass of the material contained in a thin spherical shell of radius r about a given point. For a dilute gas, which may be considered as an example of a material with no degree of order, the number of molecules in such a shell increases as r^2 and the RDF is a parabola. For a crystal the number of lattice points in the shell will be zero except for those values of r that correspond to the symmetrically placed groups of neighbouring lattice points. The RDF consists of a sequence of delta functions whose heights approach a parabolic curve at large values of r . For an amorphous material in which there is some degree of short range order the RDF will consist of a sequence of oscillations that decay to the parabolic form as r increases. The three examples of the RDF are illustrated in Fig. 1.1. For the amorphous material the RDF has merged into the parabola at a radius R whereas the crystal RDF is still a series of delta functions. The radius R provides a

measure of the finite range of the structural ordering in the amorphous material. For an ideal crystalline material the range is infinite.

The RDF can be determined by x-ray or neutron scattering. A recent determination (Sinclair and Wright, 1983) of the RDF for vitreous or amorphous quartz is shown in Fig. 1.2. The peaks at small radii are associated with the placement of the Si and O atoms in the random continuous network structure of the quartz. The RDF has reached the parabolic form at 1 nm radius. The correlations in the positions of the neighbours of the atom at the origin have vanished when the radius reaches 1 nm. This radius may be called the structural correlation radius for quartz. Its magnitude is approximately three times the average distance between silicon atoms in the amorphous quartz.

The physical properties of a material in the amorphous form may differ from those in the crystalline form because of the absence of long range order in the amorphous form. Some examples may be cited.

A characteristic property of a crystalline solid is the existence of a definite temperature, or melting point, at which the solid is transformed into a liquid. Amorphous materials do not display a definite melting temperature because of the variable bond strengths between the randomly distributed molecules. Many amorphous materials display a glass transition temperature rather than a melting temperature but this behaviour is not universal.

The resistivity of a metallic glass, such as $\text{Pd}_{0.8}\text{Si}_{0.2}$, is higher than that of the crystalline form and varies little with increasing temperature (Zallen, 1983). For the crystal the resistivity increases almost

linearly with increasing temperature as the number of phonons present to scatter the electrons, and the degree of disorder, increases. For the amorphous form the high degree of structural disorder present is not greatly increased by increase of temperature and so the resistivity is not very sensitive to temperature.

The reflectivity spectra of amorphous and crystalline germanium show differences that can be attributed to the different degrees of order present in the two forms (Zallen, 1983). Both forms are transparent in the infrared with reflectivity 0.36 and refractive index $n=4$. However, the spectrum for the crystalline form exhibits a series of sharp oscillations between 2.5 and 7.5 eV photon energies that are attributed to the electronic band structure which is a direct consequence of the long range periodic order in the crystal. The spectrum of the amorphous form varies smoothly throughout the same region.

X-ray scattering provides another example of the differences. For crystalline materials the powder x-ray diffraction pattern consists of a set of well defined rings corresponding to the Bragg reflections from the different crystal planes. For an amorphous material the rings are diffuse and rapidly decrease in intensity after the first, or smallest diameter, ring because the scattering centres lack the positional ordering present in the crystal.

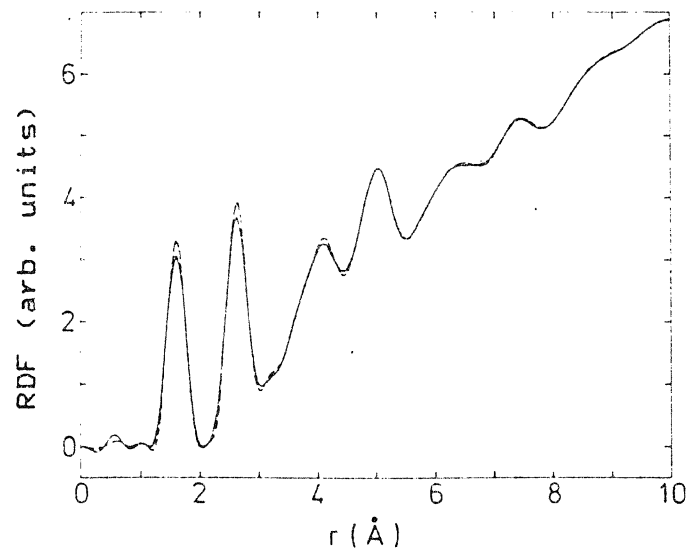
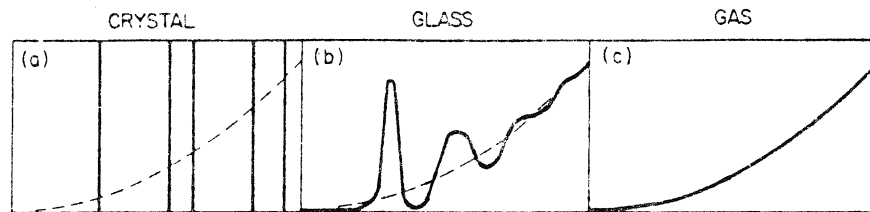
In the work that follows light scattering from three amorphous materials fused quartz, "pyrex" boro-silicate glass, and soft soda-lime silicate glass is studied. The low frequency Raman spectrum obtained in different combinations of the polarization of the incident and scattered

photons is presented for each material . The shape of the spectrum and its dependence on the polarization is compared with theoretical estimates for these materials. A measure of the structural correlation radius is obtained for each material and the form of the correlation function for the photoelastic and elastic constants in each case is examined.

The development of the experimental knowledge of the low frequency Raman spectrum in amorphous materials and the theory is presented in chapter 2. Experimental methods are described in chapter 3. The results are presented in chapter 4 and discussed in chapter 5. The conclusions are given in chapter 6.

Fig. 1.1 Radial distribution function vs radius for:
a) crystal, b) glass, c) gas.

Fig. 1.2 Radial distribution function vs radius for
fused quartz.



2- THEORY

The Raman spectrum of a material in the amorphous form differs in several respects from that of the crystalline form. The latter consists of one or more lines corresponding to the creation or annihilation of single phonons near the centre of the first Brillouin zone for the optical vibration modes of the crystal. There may also be some bands that arise from two-phonon scattering, with a net zero change in total phonon wave-vector, which can be distinguished from the one phonon bands by the temperature dependence of the scattering intensity or by a comparison of the Stokes and anti-Stokes intensity ratios. For the amorphous form the one phonon lines of the crystal are replaced by broad bands that arise from the breakdown of the selection rule that limits the one phonon lines of the crystal to zone centre phonons. For a monoatomic material, such as silicon (Smith et al, 1971), the single one phonon line of the crystalline form is replaced by a band that extends over a few hundred cm^{-1} from the exciting line and exhibits several peaks. For a material with a molecular basis, such as quartz, the spectrum in part looks like a strongly broadened and shifted form of the many one-phonon lines of the crystalline spectrum (Krishnamurti, 1958) but it may also contain a strong continuum that extends from the exciting line to several hundred cm^{-1} (Krishnan, 1953; Flubacher et al, 1959).

For many amorphous materials the spectrum below 200 cm^{-1} shift has a common feature that is not associated with any aspect of the spectrum of the crystalline material. As the Raman shift increases from about 10 cm^{-1} the intensity rises and passes through a maximum whose location and sharpness is material dependent. In a-Ge, a-Ge_{0.5}Sn_{0.5} and a-

InSb a broad peak occurs at 75, 50, and 30 cm^{-1} respectively (Lannin, 1972). In fused quartz the peak is at 50 cm^{-1} (Krishnan 1953, Flubacher et al 1959). In vitrous alkali-borates the frequency of a well-defined peak is a function of the alkali content and lies between 25 and 65 cm^{-1} (Bril, 1976). In some chalcogenide glasses containing arsenic or germanium a broad peak lies between 20 and 30 cm^{-1} (Nemanich, 1977).

Since the band occurs below the range of optical branch frequencies encountered in crystalline materials it is attributed to the effects of acoustic vibrational modes. It will be called the low-frequency band (LFB).

The intensity of the Raman spectrum of an amorphous material was calculated by Shuker and Gammon (1970) under the assumption that the correlation lengths of the vibrational modes of the material are small compared to optical wavelengths. The assumption leads to the result that one phonon scattering can be observed from all modes of vibration. That is, there is no $\mathbf{q}=\Delta\mathbf{k}\sim 0$ selection rule, where \mathbf{q} is the wavevector of the phonon and $\Delta\mathbf{k}$ is the difference between incident and scattered photon wavevectors. The Stokes component at a frequency shift ω is given by

$$I_{\beta\alpha\eta\lambda}(\omega) = \sum_b C_{\beta\alpha\eta\lambda}^b (1/\omega) [1 + n(\omega, T)] g_b(\omega) \quad (1a)$$

and the anti-Stokes component is given by

$$I_{\beta\alpha\eta\lambda}(\omega) = \sum_b C_{\beta\alpha\eta\lambda}^b (1/\omega) n(\omega, T) g_b(\omega) \quad (1b)$$

where, $n(\omega, T) = [\exp(h\omega/K_B T) - 1]^{-1}$ is the Bose factor, $C_{\beta\alpha\eta\lambda}^b$ is a coupling constant for each band of vibration b with the subscripts $\beta\alpha, \eta\lambda$

describing the polarization of the incident and scattered photons respectively, and $g_b(\omega)$ is the density of the vibrational states at frequency ω . In Eqs (1a) and (1b) the radiation factors $(\omega_L - \omega)^4$ (Stokes) and $(\omega_L + \omega)^4$ (anti-Stokes), where ω_L is the incident photon frequency, have been omitted. The coupling coefficients between the photons and the quasi-phonons in the amorphous material, as well as the density of vibrational states, are treated as parameters to be determined. In the first instance, Shuker and Gammon assumed that the coupling constant for a given vibrational band type is constant across the band. Upon removal of the temperature dependent and frequency dependent terms the density of vibrational states associated with that band can be determined. If the density of states is known, or assumed from other considerations, the coupling constant can be determined

At very low frequencies, in those cases for which the effects of the strong unmodified (Rayleigh) scattering are negligible, it has been found that LFB reduced spectrum, $I\omega / [n(\omega) + 1]$, which is proportional to the product $C^b(\omega) g(\omega)$, varies as ω^4 (Lannin, 1972, Nemanich, 1977). For the long wavelength acoustic phonons that contribute to this band the density of vibrational states will vary as ω^2 as ω approaches zero so that the coupling constant must also vary as ω^2 as $\omega \rightarrow 0$. At higher frequencies the variation must change in order to produce the observed maximum in the LFB.

Martin and Brenig (1974) presented a theoretical development of the properties of light scattered from long wavelength acoustic modes in amorphous solids. Their model is based on the assumption that light is scattered by distorted plane wave acoustic phonons in an elastic continuum.

The coupling between the phonon and the photon is determined by the classical photoelastic constants of the material and the strains arising from the acoustic phonon. An outline of the essential parts of the calculation is presented in Appendix I.

Both electrical and mechanical irregularity in the material properties were taken into account in order to derive an explicit expression for the coupling constant to second order in the spatial fluctuations of the photoelastic and elastic constants. It was assumed that all spatially fluctuating quantities in the material exhibited the same structural correlation radius (SCR). The expression was derived in terms of the average values of the appropriate combinations of photoelastic constants for the longitudinal and transverse phonon C_L , C_t , respectively, the values of their fluctuation δC_L , δC_t , the average value of the fluctuations of the elastic constants λ , the correlation length of the various fluctuations 2σ , the longitudinal and transverse speeds of sound in the material v_L , v_t , and the complex dielectric constant for a back scattering experimental configuration. In particular the correlation function for the mean square fluctuations of the photoelastic and elastic constants was taken as a Gaussian, $F(\mathbf{R}) = \exp(-R^2/R_c^2)$, where \mathbf{R} is the vector joining two volume elements at positions \mathbf{R}_1 and \mathbf{R}_2 and R_c is the SCR.

The results for the frequency dependence of the coupling constant and its dependence on the depolarization of the incident and scattered photons were consistent with the observation of the LFB in a-Si (Lannin, 1973) in the back scattering configuration. The SCR was shown to be about 0.4 nm.

Nemanich (1977) adapted the Martin and Brenig (MB) model for a study of the low-frequency 90° inelastic light scattering from chalcogenide glasses and alloys. For this case the results of the MB model and the Gaussian correlation function are as follows :

$$I_{\alpha\beta\eta\lambda}^b(\omega) \propto f(\omega) \{ B_{\beta\alpha\eta\lambda} + x^2 [g_t(x) E_{\beta\alpha\eta\lambda}^t + g_L(x) E_{\beta\alpha\eta\lambda}^L] \} \quad (2)$$

where, $x = 2\pi c (\omega / v_L) \sigma$, 2σ is the structural correlation range

$$f(\omega) = |\omega| \{ n(\omega) \theta(\omega) + [n(\omega) + 1] \theta(\omega) \}$$

$$g_L(x) = \exp(-x^2)$$

$$g_t(x) = (v_L / v_t)^5 [\exp(-x^2 (v_L / v_t)^2)]$$

$$E_{yyyy}^t \sim (2/15) C_t^2 (\delta C_t^2 / C_t^2 + \lambda)$$

$$E_{yyyy}^L \sim C_L^2 (\delta C_L^2 / C_L^2 + \lambda) + (4/45) C_t^2 (\delta C_t^2 / C_t^2 + \lambda)$$

$$E_{yzyz}^t \sim (1/10) C_t^2 (\delta C_t^2 / C_t^2 + \lambda)$$

$$E_{yzyz}^L \sim (1/15) C_t^2 (\delta C_t^2 / C_t^2 + \lambda)$$

$$(C_L / C_t) = (1/3) (p_{11} + 2p_{12}) / (p_{11} - p_{12})$$

Here ω is the frequency shift in cm^{-1} , $\theta(\omega)$ is the step function, and p_{ij} are the photoelastic constants. $B_{\beta\alpha\eta\lambda}$ is a term describing the momentum-conserving Brillouin peaks that are present even in an amorphous material. $\delta C^2 / C^2$, λ , and v_L , v_t are quantities defined in the original MB theory. The subscripts yyyy and yzyz correspond to the VV and VH polarization

spectra respectively. The symbols V and H denote vertical and horizontal polarizations respectively as measured relative to the scattering plane defined by the direction of the incident and scattered beams. The first symbol of the pair V or H refers to the incident beam and the second to the scattered. Because the MB model dealt with the long-wave acoustic phonons, the frequency region in which the above equations are valid was given by

$$(2\pi c\omega / v_{\mu})\sigma < 1 \quad (3)$$

where $\mu = L, t$. Nemanich then showed that the MB model gives the Raman coupling constant C_{VH} for the VH scattering as

$$C_{VH}(\omega) = (A/2) \omega^2 \{ 3 (v_L / v_t)^5 \exp [- (2\pi c\omega)^2 / v_t^2) \sigma^2] + 2 \exp [- (2\pi c\omega)^2 / v_L^2) \sigma^2] \} \quad (4)$$

Here A is a constant and the velocities v_t and v_L are experimental values.

The coupling constant C_{VV} for the VV scattering is :

$$C_{VV} = A\omega^2 \{ 2 (v_L / v_t)^5 \exp [(- (2\pi c\omega)^2 / v_t^2) \sigma^2] + (15M + 4/3) \exp [(- (2\pi c\omega)^2 / v_t^2) \sigma^2] \} \quad (5)$$

$$\text{Here } M = (\delta C_L^2 + \lambda C_L^2) / (\delta C_t^2 + \lambda C_t^2) \quad (6)$$

which can be measured from the experimentally determined depolarization spectrum, defined by :

$$\rho(\omega) = C_{VH} / C_{VV} \quad (7)$$

The depolarization spectrum, $\rho(\omega)$, which depends on the spatial fluctuations of the photoelastic and elastic constants as well as the correlation function, was found to be :

$$\rho = [(4/3) + 10M / (2 / 3 + g_t / g_L)]^{-1} \quad (8a)$$

Here M is the same as introduced in Eq (6), and

$$g_t / g_L = (v_L / v_t)^5 \exp (-x^2 [(v_L^2 / v_t^2) - 1]) \quad (8b)$$

where $x = 2\pi c \omega \sigma / v_L$.

Nemanich (1977) applied his results to the chalcogenide glasses As_2S_3 , GeS_2 , $GeSe_2$, and As_2Se_3 and to the glass alloy system $(As_2S_3)_{1-x}(GeS_2)_x$. He found that the Raman coupling constant exhibited an ω^2 frequency dependence in the limit $\omega \rightarrow 0$. By fitting the predicted spectra of the model to the experimentally obtained spectra, the SCRs of the As_2Se_3 and As_2S_3 glasses were 0.65 nm, while those of the GeS_2 and $GeSe_2$ were 0.85 nm. He showed good fits of the theory to the experimental VH and VV spectra up to the top of the LFB peak after which there was a sharp deviation between the theory and the experiment. The predicted depolarization ratio was found to deviate significantly from the experimental values.

The MB theory with a Gaussian correlation function was used by Lorosch et al (1984) in a study of a series of binary glasses $B_2O_3 - xJ_2O$, with $J = Li, Na, K, Rb, Cs$, and Tl . The theory gave a very good fit to their experimental coupling constant up to the LFB peak but the theoretical values fell sharply below the experimental values for

frequencies above the peak. Their depolarization ratio spectra did not agree very well with the calculated spectra.

Malinovsky and Soklov (1986) took the MB theory with a correlation function

$$F(\mathbf{R}) = \exp (-|\mathbf{R}| / R_c) \quad (9a)$$

$$\text{where} \quad R_c = v_t / \pi c \omega_0 \quad (9b)$$

is the structural correlation radius.

They quote the result for the coupling constant C_{VH} as :

$$C_{VH} = (D / 2) \left\{ 3 \omega^2 / (\omega^2 + \omega_0^2)^2 + 2 (v_t / v_L)^5 \omega^2 / (\omega^2 + (\omega_0 v_L / v_t)^2)^2 \right\} \quad (10)$$

where D is a constant.

The coupling constant C_{VV} is :

$$C_{VV} = D \left\{ 2 \omega^2 / (\omega^2 + \omega_0^2)^2 + (15M + 4 / 3) (v_t / v_L)^5 \omega^2 / (\omega^2 + \omega_0^2 (v_L / v_t)^2)^2 \right\} \quad (11)$$

where M is given by Eq (6) and it is measured from the experimentally determined depolarization spectrum, defined by Eq (8a) with

$$g_t / g_L = (v_L / v_t)^5 \left\{ \omega^2 + (\omega_0 v_L / v_t)^2 / (\omega^2 + \omega_0^2) \right\}^2 \quad (11b)$$

Notice that it was valid to use the expression (8a) for ρ in Eq (11b) because ρ depends only on the fluctuations of the photoelastic and elastic constants and the choice of g_t and g_L .

A third function, a Lorentzian form,

$$F(R) = (1 + R^2 / R_c^2)^{-1} \quad (12)$$

was also considered by the same authors. The results for the coupling constant C_{VV} is given by :

$$C_{VV} = G \omega \left\{ 2 (v_L / v_t)^5 \exp(-\omega / \omega_0) + (15M + 4/3) \exp(-\omega v_t / \omega_0 v_L) \right\} \quad (13)$$

and for the C_{VH} coupling constant is given by :

$$C_{VH} = (G / 2) \omega \left\{ 3 (v_L / v_t)^5 \exp(-\omega / \omega_0) + 2 \exp(-\omega v_t / \omega_0 v_L) \right\} \quad (14)$$

where G is a constant.

The quantity M in Eq (13) is given by Eq (6) and it can be estimated from the experimental depolarization ratio defined by Eq (7). The prediction of the depolarization ratio is given by Eq (8a) with

$$g_t / g_L = (v_L / v_t)^5 \exp \left\{ (-\omega / \omega_0) (v_L / v_t - 1) \right\} \quad (15)$$

For the Lorentzian form of correlation function the coupling constant varies linearly with ω as the Raman frequency shift approaches zero but for both Gaussian and Poisson type of correlation functions the variation goes as ω^2 . For each form there is a maximum in the coupling constant at a frequency from which the structural correlation radius (SCR) can be measured.

Malinovsky and Sokolov (1986) in a study of several glasses: As_2O_3 , $\text{Bi}_4\text{Si}_3\text{O}_{12}$, SiO_2 , B_2O_3 , Li_2O , and GeS_2 were able to show that the coupling constant C_{VH} had the same form for each glass when plotted versus ω/ω_0 , where ω_0 is the frequency of the peak of the LFB. They concluded that glasses have a slower variation in the decrease of the correlations than monoatomic semiconductors such as silicon. They also claimed that there is a universal correlation function for glassy materials, $F(\mathbf{R}) = \exp(-|\mathbf{R}|/R_c)$, which corresponds to the structure of a continuous net-work of ordered microregions of diameter $\sim 2R_c$, where $R_c = v/2\pi c\omega_0$ is nearly constant for different glasses. They rejected the Lorentzian form on the basis of poor fit below the maximum of LFB and rejected the Gaussian form for poor fit above the maximum. Malinovsky et al (1987) also examined the changes in the LFB in going from the liquid to the glassy state in glycerine and again they found that the Poisson correlation function gave the best fit for the VH coupling constant of the LFB.

In this research it was intended to examine the Raman spectra of three available amorphous materials and to test the claims of Malinovsky and Sokolov (1986) in respect of the universality of fit of the low frequency Raman scattering, or the LFB, (in the frequency region up to 100 cm^{-1}) to the Poisson correlation function and also to further test the validity of the Gaussian and Lorentzian functions for both VV and VH polarizations. Commercially available fused quartz, pyrex boro-silicate glass, and a soft soda-lime silicate glass were chosen for this purpose.

3- EXPERIMENTAL METHODS

Raman spectra were obtained at room temperature using a Jarrell-Ash 1m double monochromator with 1180 lines per mm gratings operating in second order with dispersion 0.40 nm per mm. The gratings were driven by a synchronous motor, gear train and sine bar at a speed determined by a manually selected gear ratio. The scan on and off control, the scan direction and the data collection were under computer control. An EMI 9502B photomultiplier, cooled to $-25\text{ }^{\circ}\text{C}$ by a thermoelectric refrigerator, was used as a detector in the photon counting mode. By means of a selection signal taken from the grating drive, the spectral data were recorded digitally in channels of spectral width adjustable from 0.0125 to 0.10 nm, corresponding to frequency widths 0.5 to 4.0 cm^{-1} approximately, and variable in increments of 0.0125 nm. The spectra could also be displayed on a chart recorder. The spectra were excited by using the 488 nm or the 514.5 nm lines from a Coherent Radiation argon-ion laser at powers up to 550 mW.

The polarization of the incident beam at the sample was adjusted by a half-wave plate and checked by observation of the strongly polarized symmetric vibration of liquid CCl_4 at 458.4 cm^{-1} shift. A polaroid sheet was used as an analyzer in the scattered beam. The polarization dependence of the monochromator transmission was eliminated by placing a polarization scrambler between the analyzer and the entrance slit. The variation of the sensitivity of the detection system between Raman shifts of $\pm 157\text{ cm}^{-1}$ from the 488 nm exciting line was measured by a comparison of the intensities of the Stokes and anti-Stokes

157 cm^{-1} Raman lines of a calcite crystal after correction for the temperature factors and the spectral frequency ratio of the lines.

The materials used in this research were vitreous quartz (supplied by G.M Associates Inc, California), Pyrex boro-silicate glass 7740 (supplied by Corning Glass Works, Corning, New York) and a soft soda-lime silicate glass of unknown origin. The specimens were cylindrical rods of length 10 cm and diameters of 8 mm, 10 mm, and 10 mm respectively.

The specimens were mounted vertically so that the incident beam was directed downwards along the cylinder axis. The scattered light was collected at 90° through the side of the specimen by a collecting lens of aperture f2. A parasitic light problem was encountered in the early stages of the work, but it was greatly reduced by placing the rod in a close-fitting black cloth material case. The case had two holes for the incident and the scattered beams. As a further precautionary measure, the interior walls of the chamber that contained the specimen and the illuminating and collecting optics were covered with black cloth.

The Stokes and anti-Stokes Raman spectra were recorded at room temperature for the VV and VH polarizations for the three materials. For quartz and pyrex glass 488 nm excitation was used at an average power level of about 550 mW and a slit width of 100 μm or 1.6 cm^{-1} . When observing the Raman spectrum for the soda-lime glass, excitation at 514.5 nm with an average power of about 660 mW was used. This excitation was used because of a weak fluorescence at 488 nm which masked the Raman Stokes spectrum. An anti-Stokes spectrum in the VH polarization was

recorded for the 488 nm excitation line. The slit width was 100 μm . All spectra were recorded in channels of width 0.10 nm corresponding to $\sim 4.0 \text{ cm}^{-1}$. The scan speed used for data collection was 0.25 nm per min so that the integration time per channel was $\sim 25 \text{ sec}$. When displaying the spectra on the chart recorder the maximum count rate was 2×10^3 counts per second and the chart speed was 2.5 mm per min. Intensity data were smoothed with a seven point formula. In order to determine the wavelength corresponding to a given channel, and thereby to calculate the corresponding wave-number shift, the Hg 419.6 nm (150 cm^{-1} shift) was used as the reference standard. The background intensity for the spectra were estimated by recording the intensities of the anti-Stokes lines to the point at which the scattered intensity vanished. On the Stokes side the extent of the bands was such that the scattering was appreciable at shifts of 600 cm^{-1} .

The experimental x-ray diffraction patterns between $2\theta = 25^\circ$ and $2\theta = 55^\circ$ for the three materials which were obtained by using the copper K_α line ($\lambda=0.154 \text{ nm}$) did not show any peaks. The height of the diffraction peaks when they exist is determined by the percentage of the crystalline phase in the glass. Since the x-ray machine used had a background noise level of about 3% and no peaks were observed above this level we conclude that the percentage of crystalline regions in our glasses, if any, is less than 3%. Another possibility is that the glass consists of very small microcrystalline regions which will produce very broad bands with low intensity; however, our experimental results did not show any broad bands above the 3% noise level. Therefore, such small microcrystalline regions were not present in sufficient concentration to be detected.

4- RESULTS

i) "Pyrex" boro-silicate glass:

Fig. 4.1 shows the smoothed VV and VH Stokes spectra which were obtained at room temperature and Fig. 4.2 shows the anti-Stokes VV spectrum for pyrex glass. In a crystalline material broad bands with the two peaks could be the result of a mixture of one and two-phonon scattering. Two phonon scattering in amorphous materials has been reported (Lannin and Carroll, 1982). The two processes are distinguished by their temperature dependence or, equivalently, by the ratio of the Stokes to the anti-Stokes scattering intensities at the same temperature. From Eq (1) the anti-Stokes VV spectrum, with the additional correction factors for the actual frequency of the scattered anti-Stokes and Stokes photons and the measured frequency dependence of the response function of the detection system can be calculated. The fit of the calculated VV anti-Stokes spectrum to the experimental data is shown in Fig. 4.3. The good fit is sufficient evidence that below 200 cm^{-1} the bands are the result of a one-phonon process or first order scattering. Fig.4.1 also shows that the depolarization factor $\rho = (I_{VH} / I_{VV})$ varies across the bands. At the low-frequency end the band appears to be depolarized with a depolarization ratio of 0.53 at the peak of the LFB ($\omega = 46 \text{ cm}^{-1}$). The depolarization ratio then decreases to reach a value of 0.061 at the top of the second peak ($\omega = 440 \text{ cm}^{-1}$).

The results of Nemanich (1977) based on the Martin and Brenig model with a Gaussian correlation function $F(R) = \exp(-R^2 / R_c^2)$ can be applied to our experimental data. Throughout our comparison of the

theoretical predictions with the experimental data we will be using the reduced spectrum $I_{\text{exp}} / (\omega (n(\omega) + 1))$ which is equal to the coupling constant $C_{ij}(\omega)$ for a Debye vibration spectrum. Fig.4.4 shows the reduced VV and VH spectra for the pyrex.

The theoretical VH spectrum is given by Eq (4). Fig. 4.5 shows the fit of this equation to the experimental reduced spectrum for the frequency region ($\omega = 20$ to 350 cm^{-1}), where the values of $v_t = 3.37 \times 10^5 \text{ cm / s}$ and $v_L = 5.52 \times 10^5 \text{ cm / s}$ were obtained from Brillouin scattering (Shapiro et al, 1966). The fit for $\omega \leq 43 \text{ cm}^{-1}$ is good but a strong deviation from the experimental data is observed at $\omega > 43 \text{ cm}^{-1}$. The value of σ obtained to fit the experimental VH spectrum and that obtained using Eq (4) at the maximum of the LFB was $4.5 \times 10^{-8} \text{ cm}$ or $R_c = 9.0 \times 10^{-8} \text{ cm}$. According to Eq (3) this value σ indicates that the long-wavelength limit applies only for $\omega < 40 \text{ cm}^{-1}$. Therefore, the deviation between the experimental and the predicted VH spectrum occurs where the MB model is no longer expected to apply if the criterion $(2\pi c \omega \sigma / v) < 1$ is applied rigourously. The value of σ can be theoretically predicted from Eq (4). The first term of Eq 4, $\omega^2 (\exp(-(2\pi c \omega \sigma / v)^2))$ has a maximum at

$$\omega_0 = (v / 2\pi c \sigma) \quad (16)$$

Since for VH scattering the intensity is dominated by the transverse acoustic modes, the structural correlation range (2σ) can be predicted using Eq (16) with $v = v_t$. Here $\omega_0 = 43 \text{ cm}^{-1}$ is the peak of the LFB and $v_t = 3.37 \times 10^5 \text{ cm / s}$. The predicted value of 2σ is $= 8.3 \times 10^{-8} \text{ cm}$ which

agrees with the experimental value 9.0×10^{-8} cm within experimental error.

The fit of the theoretical VV spectrum given by Eq (5) to the experimental values is shown in Fig.4.6. The quantity M in the equation can not be directly measured but it can be determined from the experimentally obtained depolarization. There is a reasonable fit in Fig. 4.6 for $\omega \leq 43 \text{ cm}^{-1}$ but there is a strong deviation for $\omega > 43 \text{ cm}^{-1}$. A part of this deviation may be ascribed to the frequency limitations of the MB theory but it is clear that the VV spectrum extends to much higher frequencies than the VH spectrum. Contributions from vibrational modes that are not describable by an elastic continuum model must be important so that the MB model is of limited value in this case. As for the VH spectrum, the value of $\sigma = 4.5 \times 10^{-8}$ cm provides a fit of the theory to the data for $\omega \leq 43 \text{ cm}^{-1}$. Since for the VV scattering longitudinal and transverse modes have almost the same contribution to the scattering intensity, the structural correlation range can be estimated from Eq (13) with v being the average of the longitudinal and transverse velocities of the acoustic waves. The predicted value of σ is 5.5×10^{-8} cm.

Fig. 4.7 shows the fit of Eq (8) to the experimental depolarization ratio spectrum. The quantity M in the equation is scaled to yield agreement with the experimental ρ at the frequency shift of the LFB peak. Fig. 4.7 shows that Eq (8) does not fit the experimental values and also the shapes of the spectra are different. Although, the same value of $M = 0.30$ was found to fit both the VV and depolarization spectra, there is a considerable difference in their fit to the experimental data. This difference is due to the higher sensitivity of the depolarization to the value

of M compared to that of the VV spectrum. The predicted values of ρ have a maximum difference of about 23% from experimental values in the region $\omega \leq 43 \text{ cm}^{-1}$.

The results of Malinovsky and Sokolov (1986) based on the MB theory with a Poisson correlation function, $F(R) = \exp(-|R|/R_c)$, can be applied to our experimental data. Fig 4.8 shows the low-frequency VH spectrum fitted to Eq (10). The value of ω_0 in the equation is adjusted to give agreement with the experimental spectrum at the top of the LFB peak. Fig. 4.8 shows a good fit throughout the region of interest (20 to 100 cm^{-1}). The structural correlation radius is given by $R_c = (v / \pi c \omega_0)$, where $v = 3.37 \times 10^5 \text{ cm/s}$ is the velocity of the transverse acoustic waves and $\omega_0 = 43 \text{ cm}^{-1}$ is the LFB peak frequency shift, so $R_c = 8.3 \times 10^{-8} \text{ cm}$. Fig. 4.9 shows the fit of the VV spectrum given by Eq (11) to the experimental spectrum, where the quantity M in the equation is measured from the experimental depolarization. The figure shows a good fit not only in the region of interest but also out to about 350 cm^{-1} . As for the VH spectrum, the value of $\omega_0 = 43 \text{ cm}^{-1}$ provides a good fit of the theory to the data for $\omega \leq 43 \text{ cm}^{-1}$. Fig. 4.10 shows that the predicted ρ using Eq (8a), with (g_t / g_L) given by Eq (11b), does not fit the experimental depolarization spectrum. The quantity M was scaled to give agreement with the experimental values at the peak of LFB peak. The value of $M = 2.2$ was found to fit the depolarization and the VV spectra to Eqs (8a) and (11a) respectively. The predicted VV spectrum is not very sensitive to the value of M .

The results of the Lorentzian correlation function can also be applied to our experimental data. The fit of Eq (14) with $\omega_0 = 43 \text{ cm}^{-1}$ to

the experimental VH spectrum is shown in Fig. 4.11. The theory provides a poor fit for $\omega < 43 \text{ cm}^{-1}$ but the fit is good for $43 \leq \omega \leq 200 \text{ cm}^{-1}$. Fig. 4.12 shows the fit of Eq (13) to the experimental spectrum. As for the VH spectrum, the value of $\omega_0 = 43 \text{ cm}^{-1}$, and the $\text{SCR} = 5.2 \times 10^{-8} \text{ cm}$, provided the agreement between the theory and experimental data at the peak of the LFB. The fit in Fig. 4.12 is good for the region $43 \leq \omega \leq 120 \text{ cm}^{-1}$ but the experimental values fall below the theoretical values for $\omega < 43 \text{ cm}^{-1}$. Fig. 4.13 shows the fit of Eq (8a), with (g_t / g_L) given by Eq (15), to the experimental depolarization ratio. The same value of $M = 0.36$ fitted both ρ and the VV spectra to their experimental counterparts at the peak of the LFB. The predicted values of ρ are within 20% from the experimental values for $\omega < 43 \text{ cm}^{-1}$ but this difference is only about 5% for $43 \leq \omega \leq 120 \text{ cm}^{-1}$.

Fig. 4.1 Pyrex VV and VH experimental intensity (arb. units) vs Raman shift (cm^{-1}).

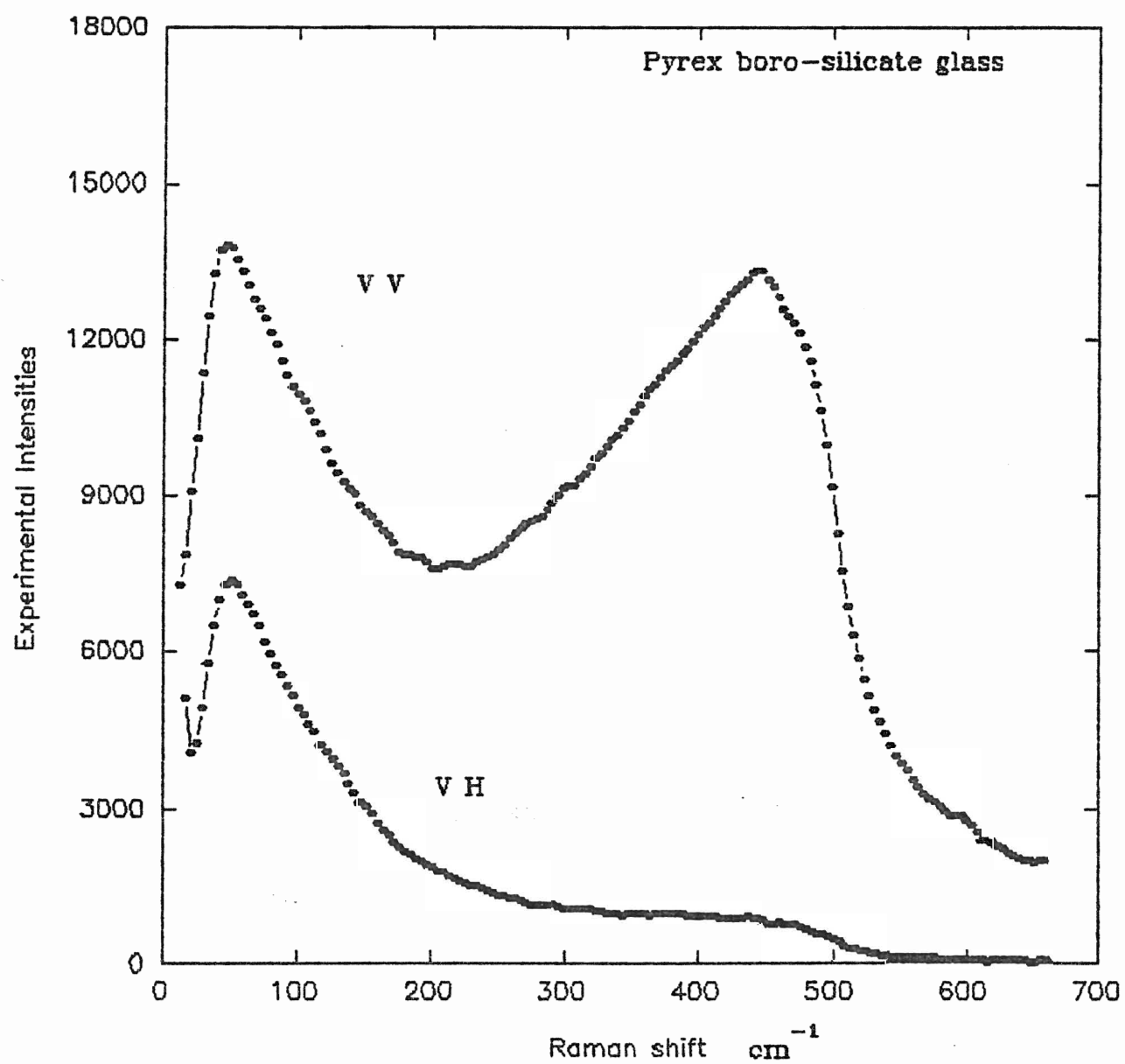


Fig. 4.2 Pyrex experimental anti-Stokes VV intensity (arb. units) vs Raman shift (cm^{-1}).

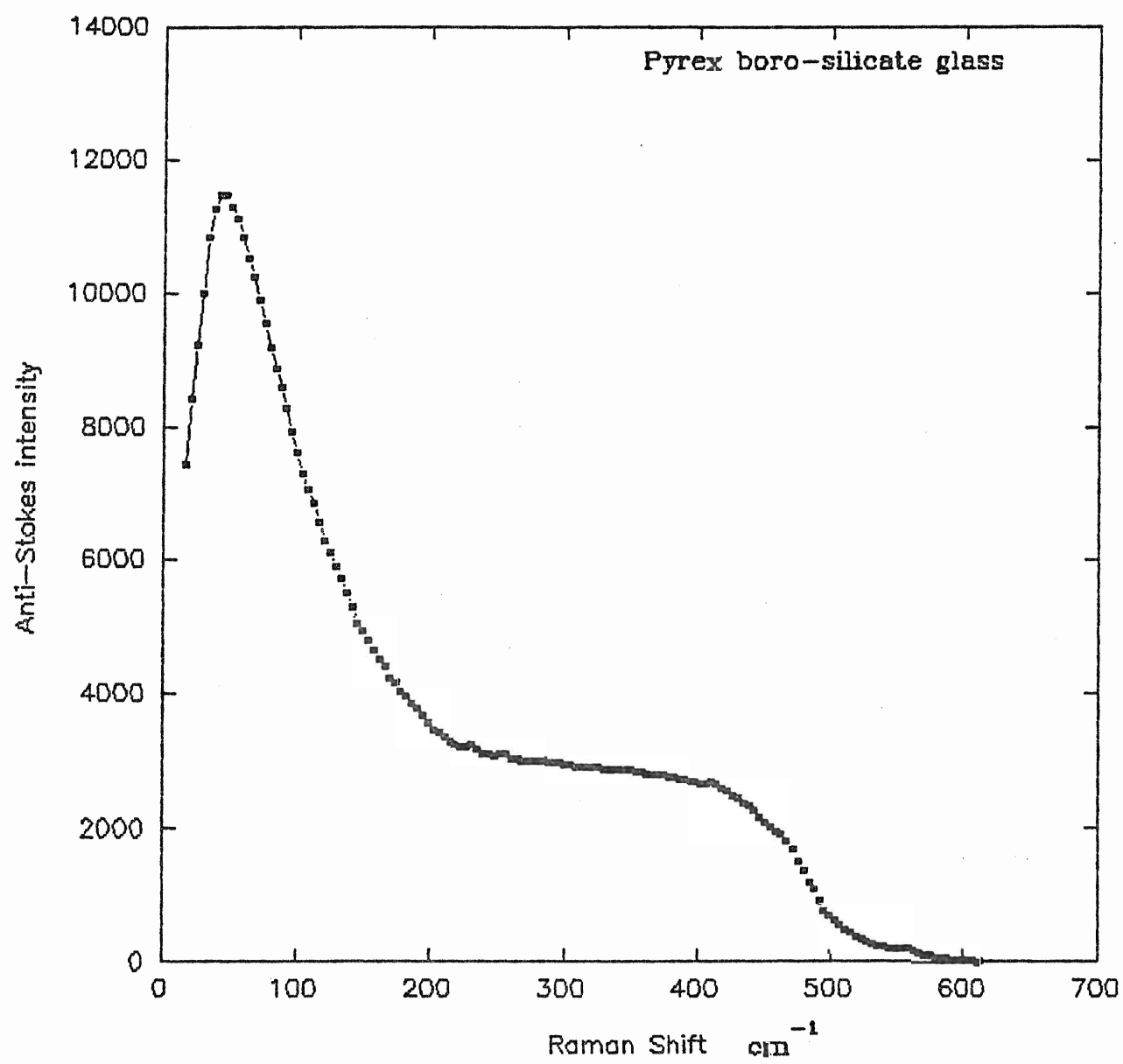


Fig. 4.3 Pyrex predicted and experimental anti-Stokes VV intensity (arb. units) vs Raman shift (cm^{-1}).

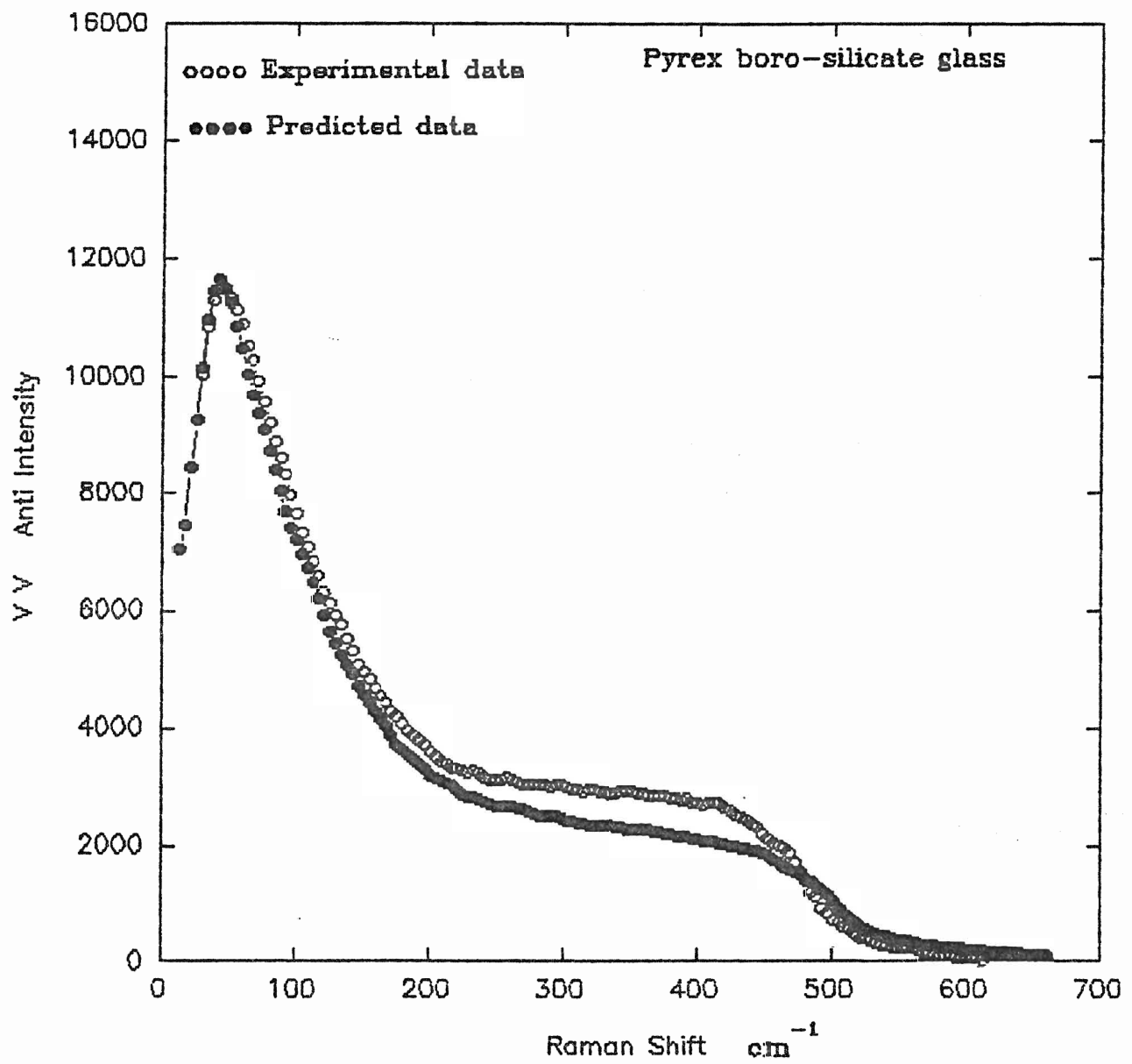


Fig. 4.4 Pyrex experimental VV and VH reduced spectra
(arb. units) vs Raman shift (cm^{-1}).

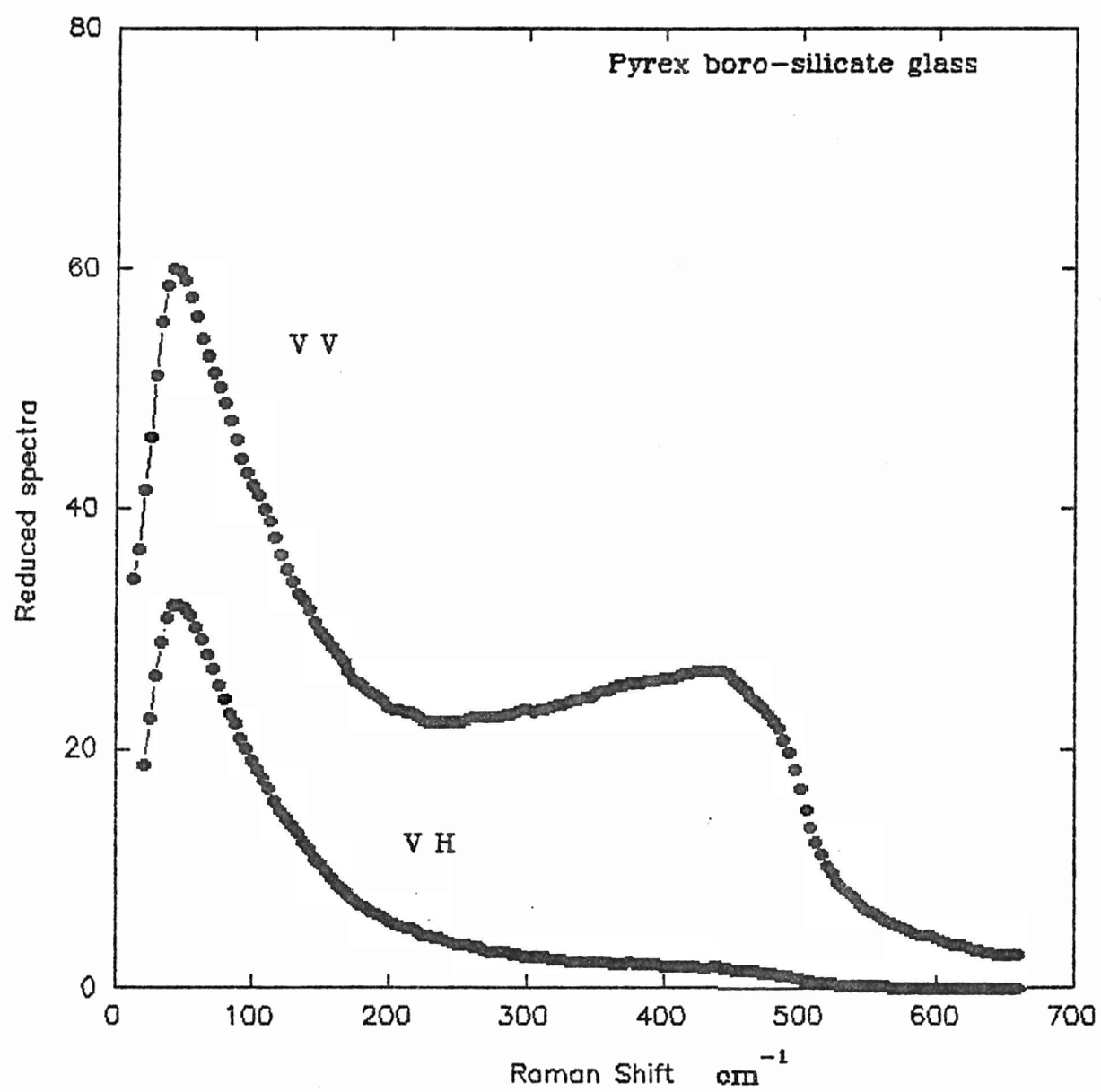


Fig. 4.5 Pyrex experimental and Gaussian predicted VH reduced spectrum (arb. units) vs Raman shift (cm^{-1}).

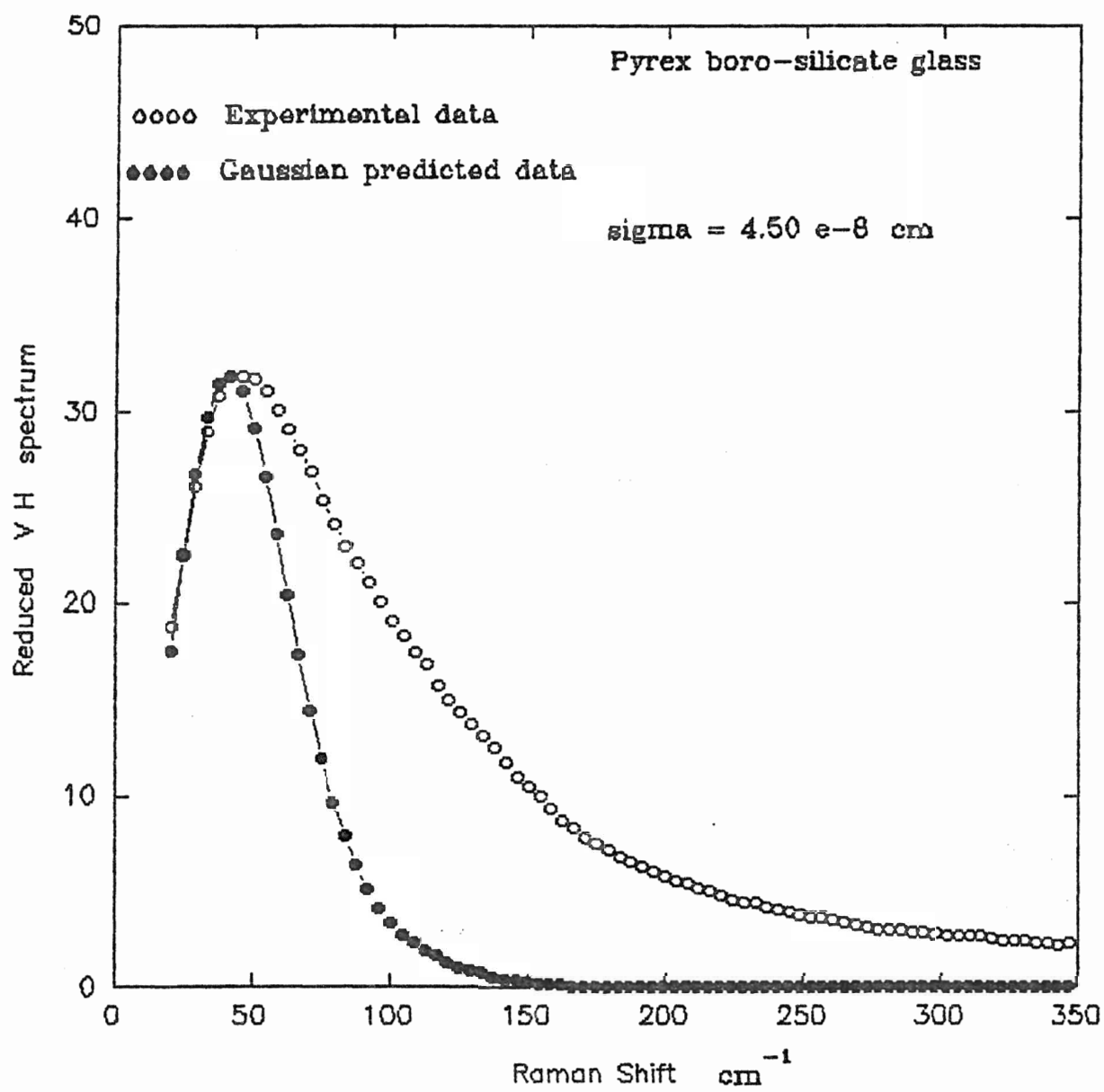


Fig. 4.6 Pyrex experimental and Gaussian predicted VV reduced spectrum (arb.units) vs Raman shift (cm^{-1}).

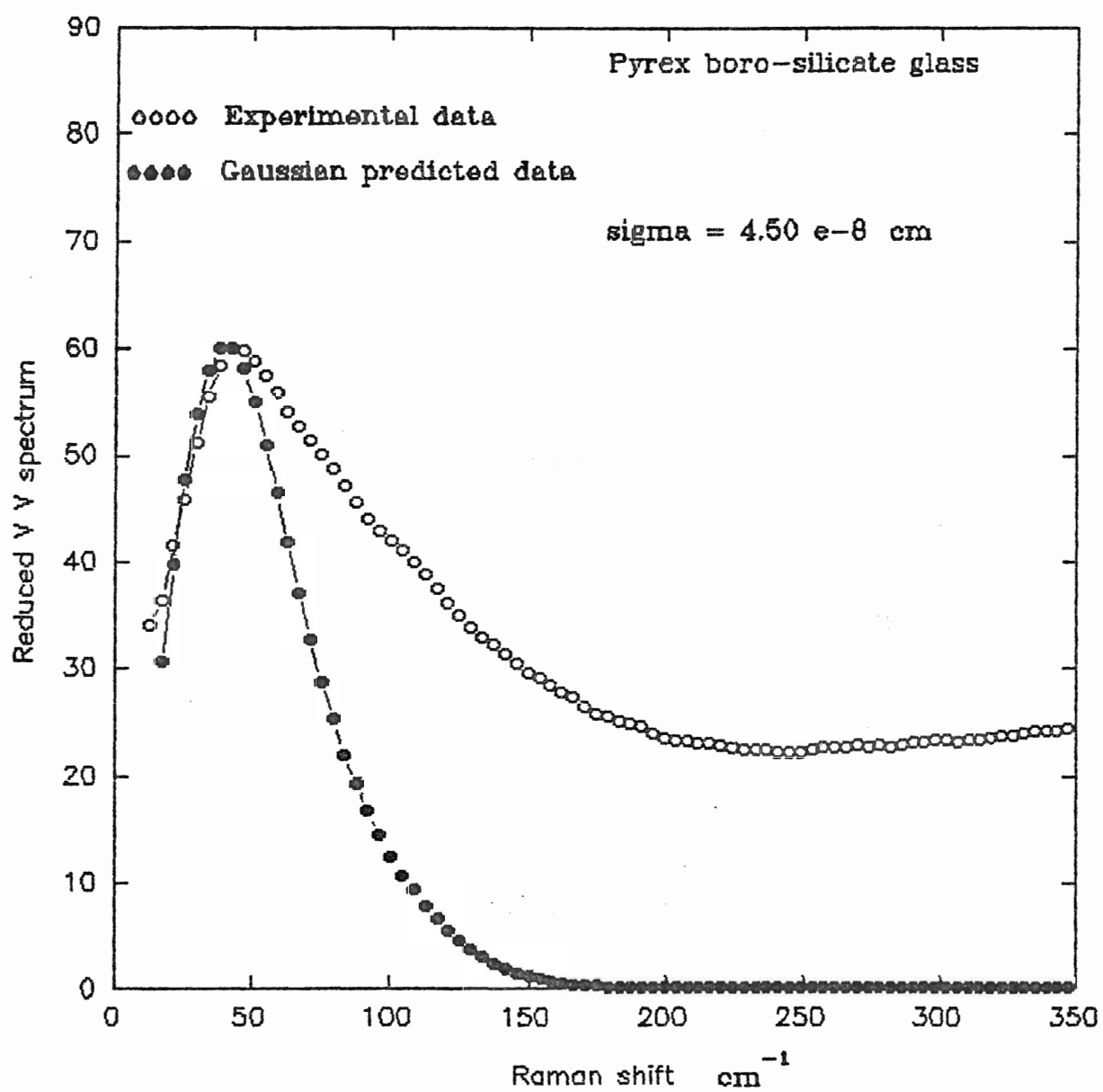


Fig. 4.7 Pyrex experimental and Gaussain predicted depolarization ratio spectrum vs Raman shift (cm^{-1}).

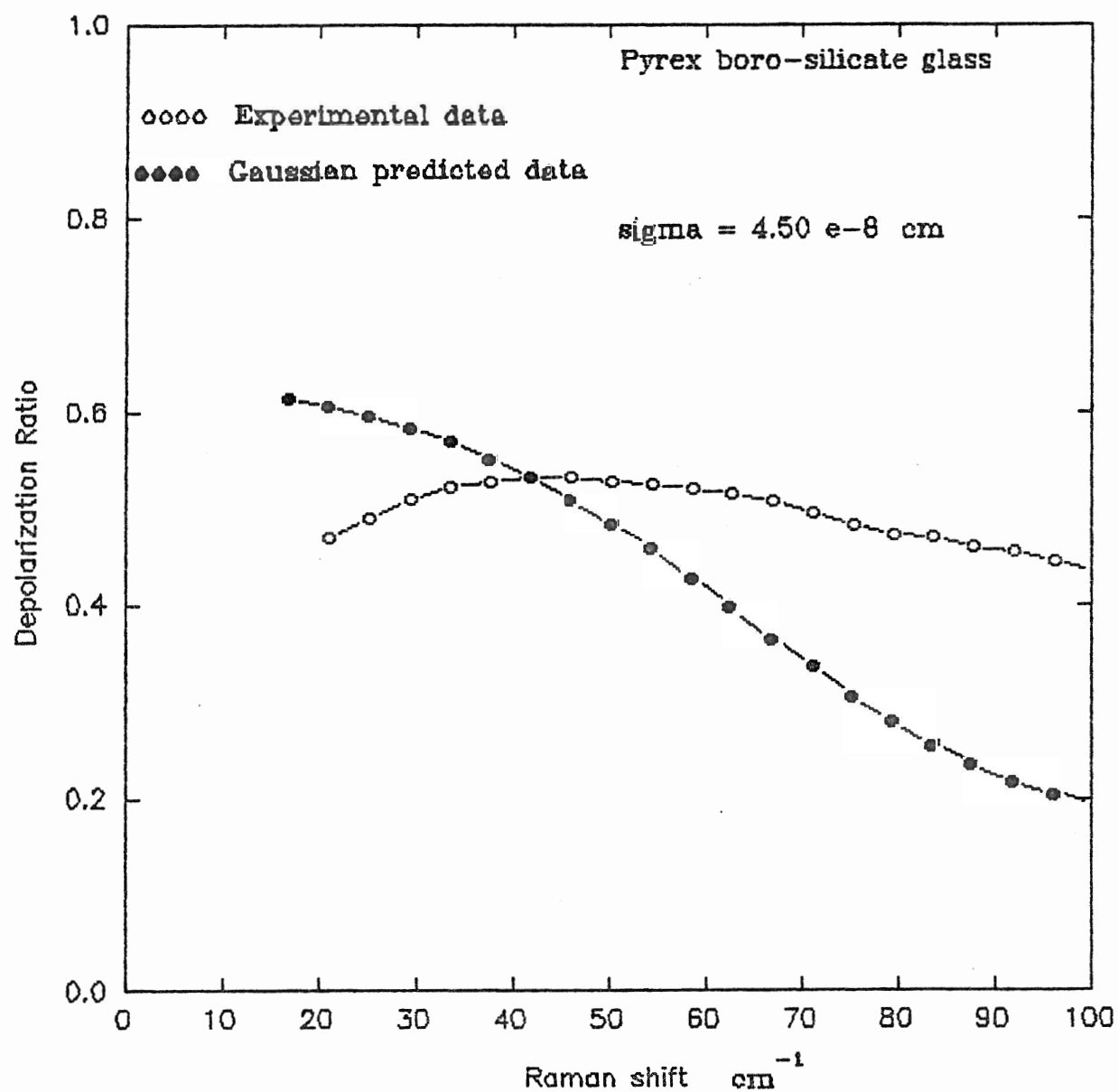


Fig. 4.8 Pyrex experimental and Poisson predicted VH reduced spectrum (arb. units) vs Raman shift (cm^{-1}).

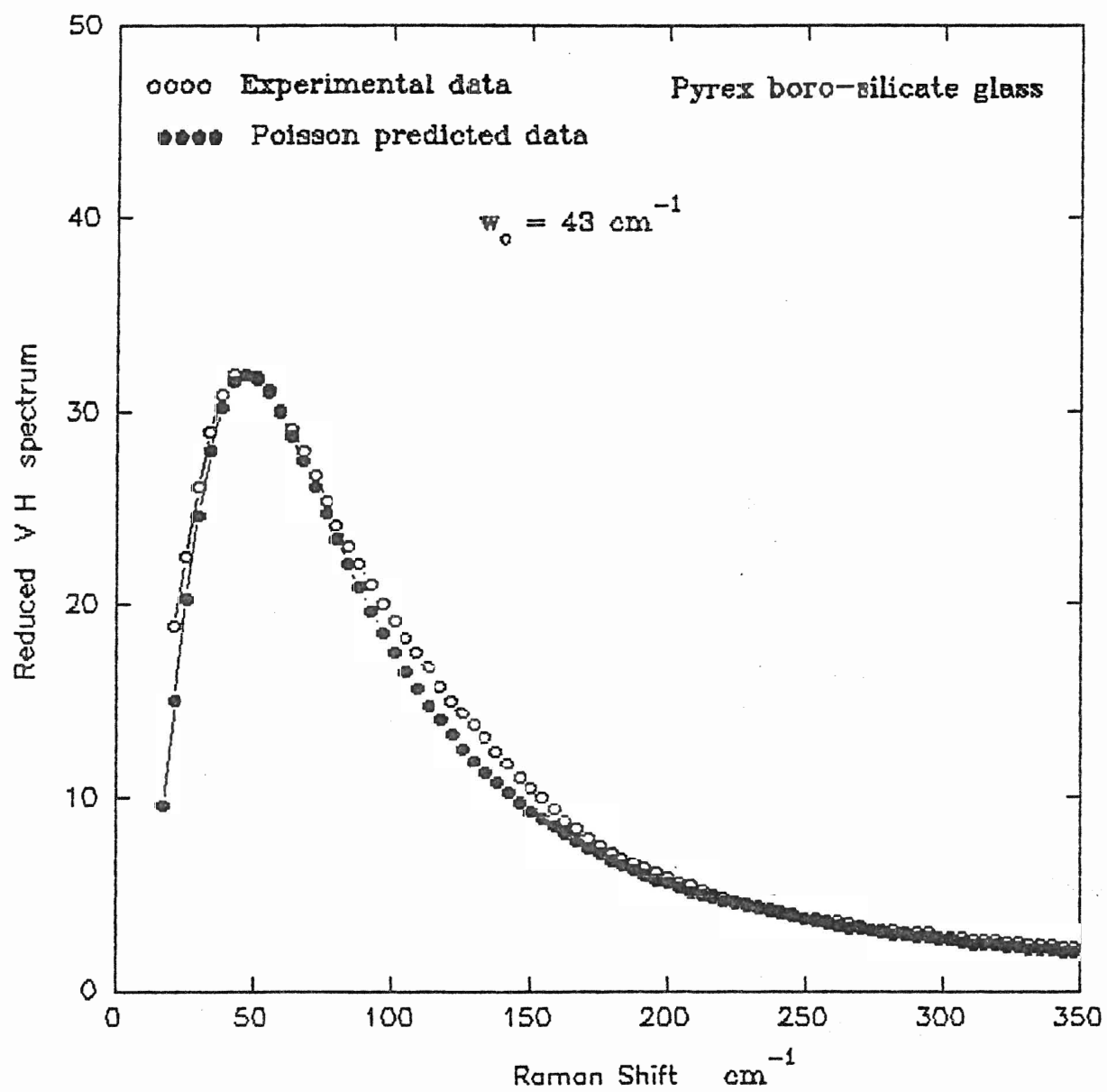


Fig. 4.9 Pyrex experimental and Poisson predicted VV reduced spectrum (arb. units) vs Raman shift (cm^{-1}).

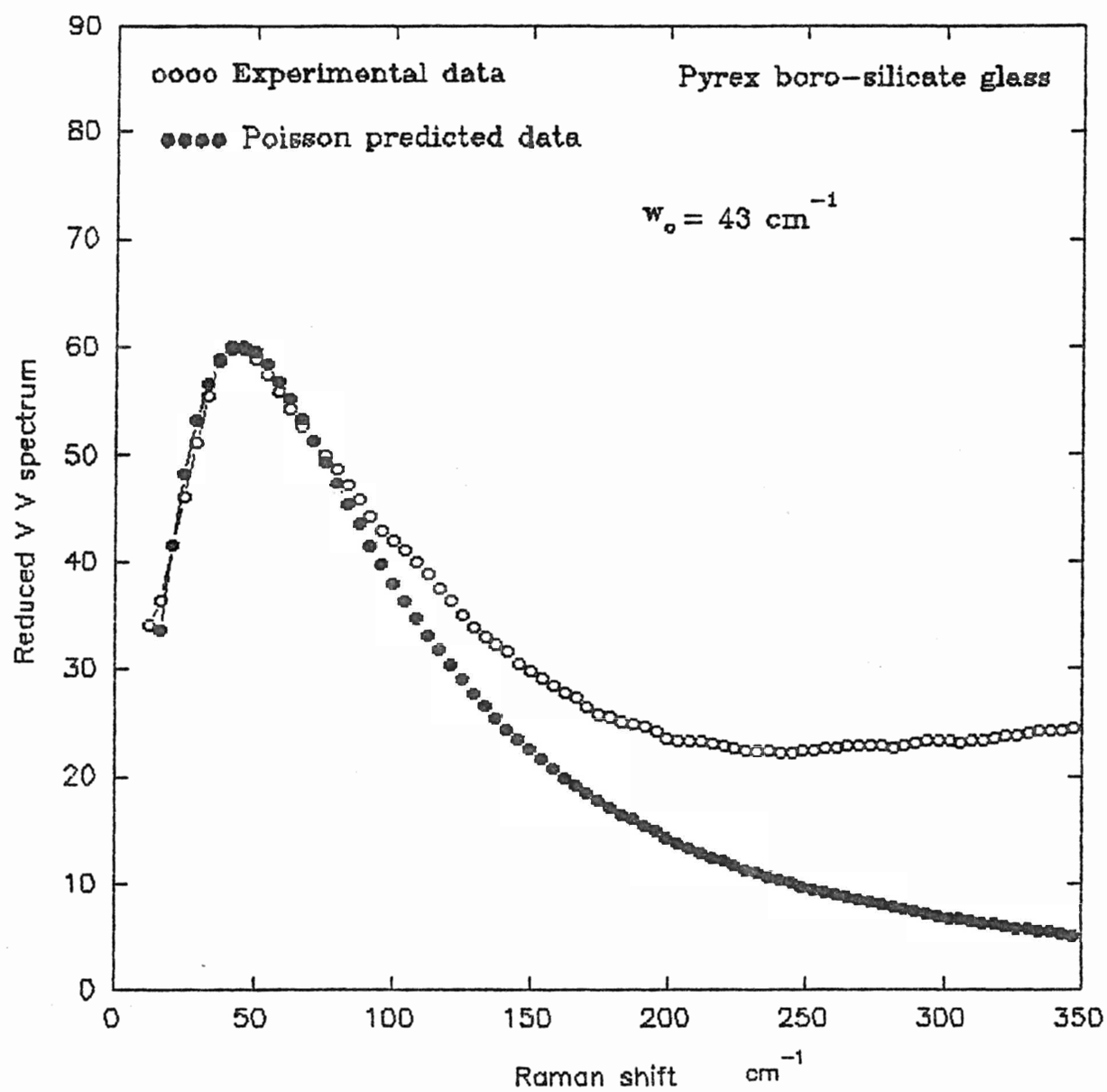


Fig. 4.10 Pyrex experimental and Poisson predicted depolarization ratio spectrum vs Raman shift (cm^{-1}).

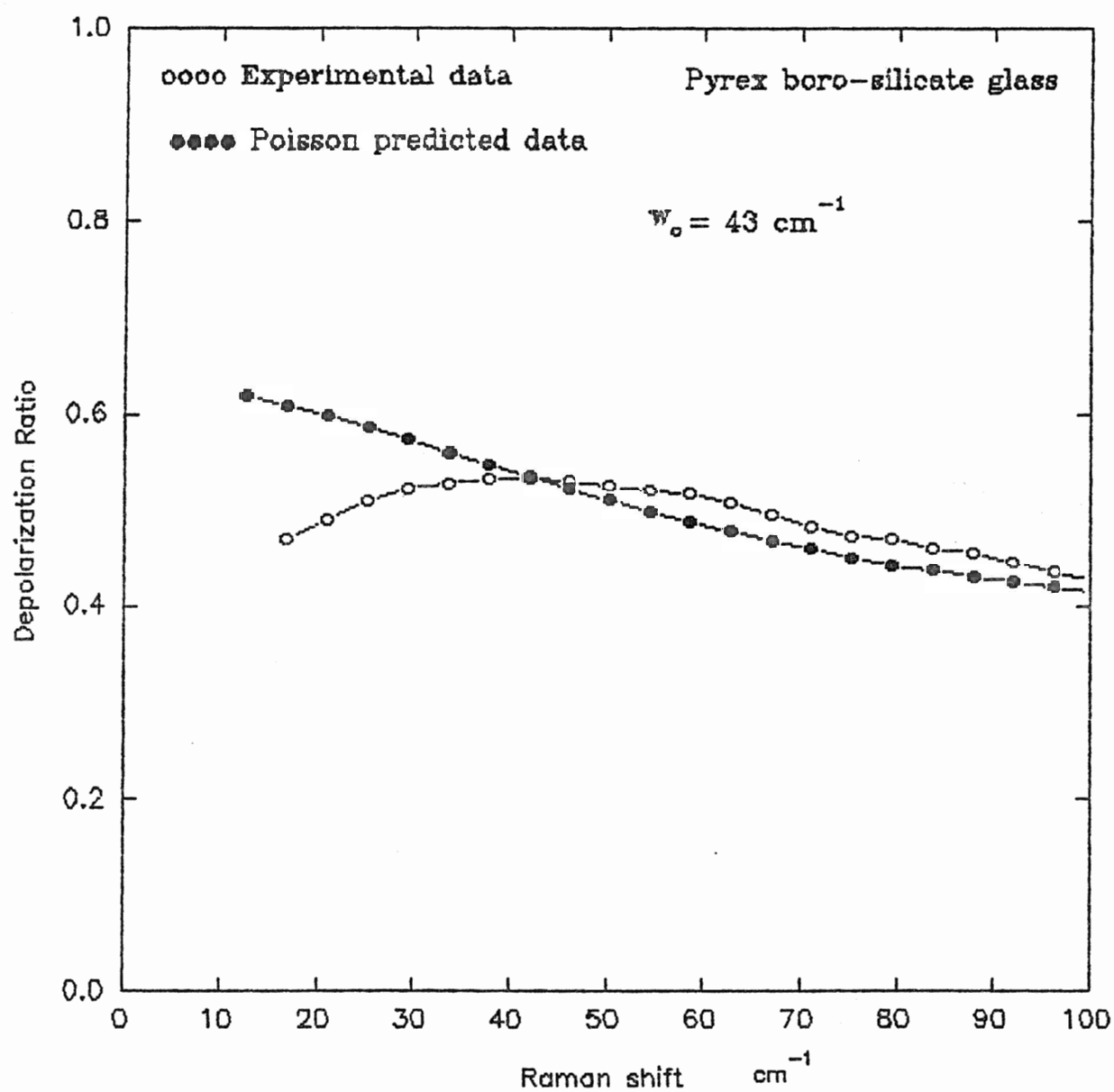


Fig. 4.11 Pyrex experimental and Lorentzian predicted VH reduced spectrum (arb. units) vs Raman shift (cm^{-1}).

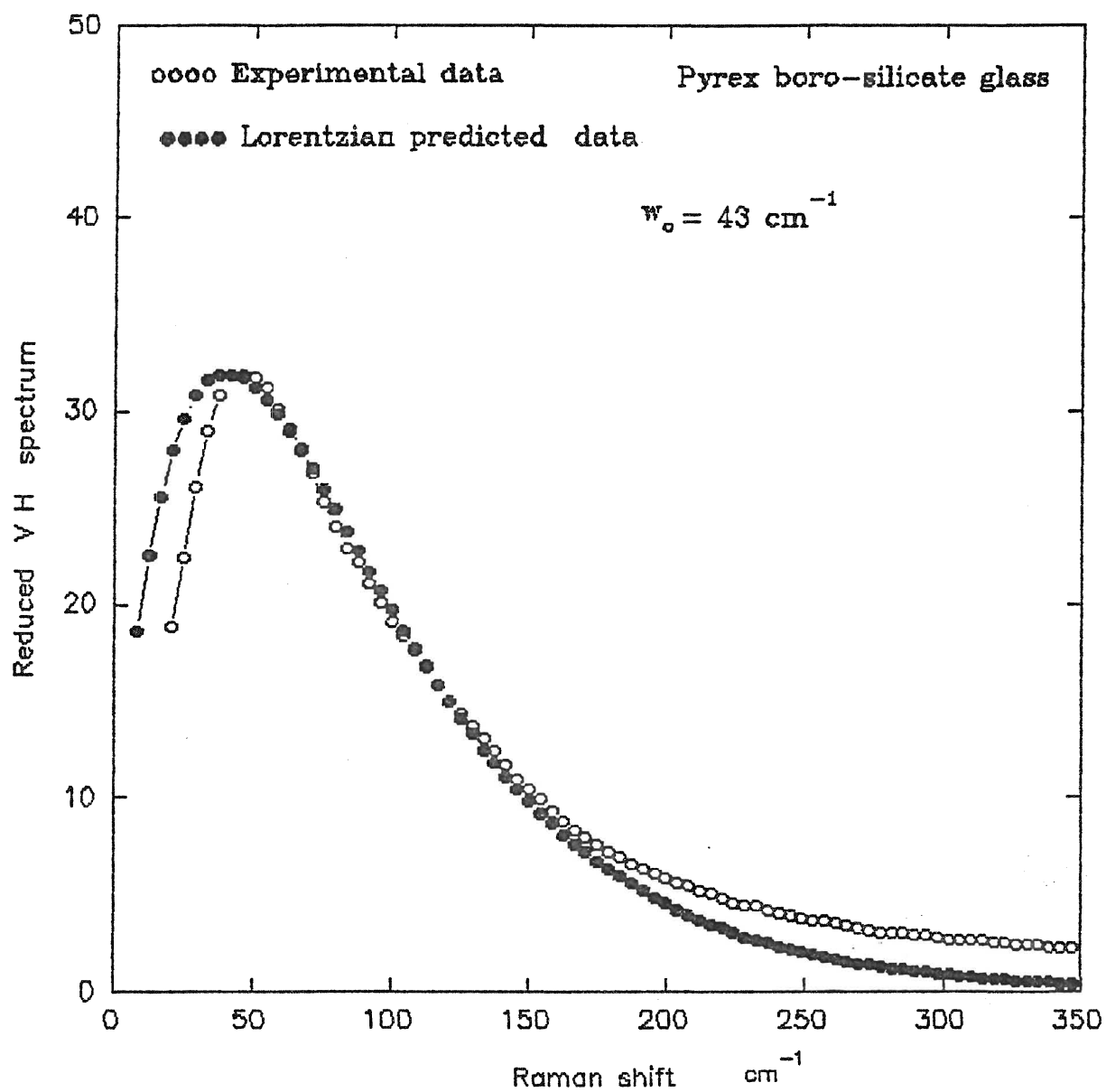


Fig. 4.12 Pyrex experimental and Lorentzian predicted VV reduced spectrum (arb. units) vs Raman shift (cm^{-1}).

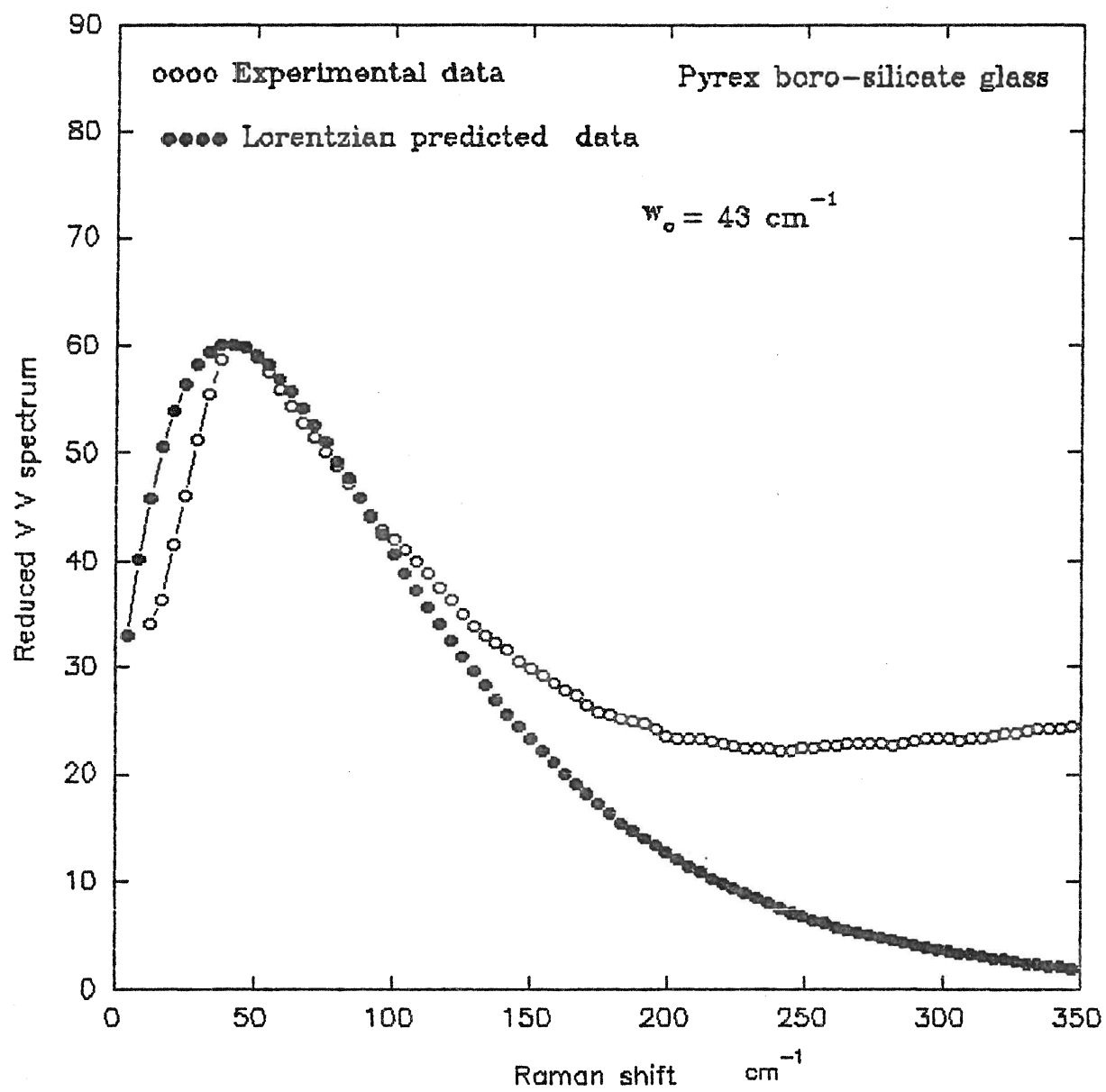
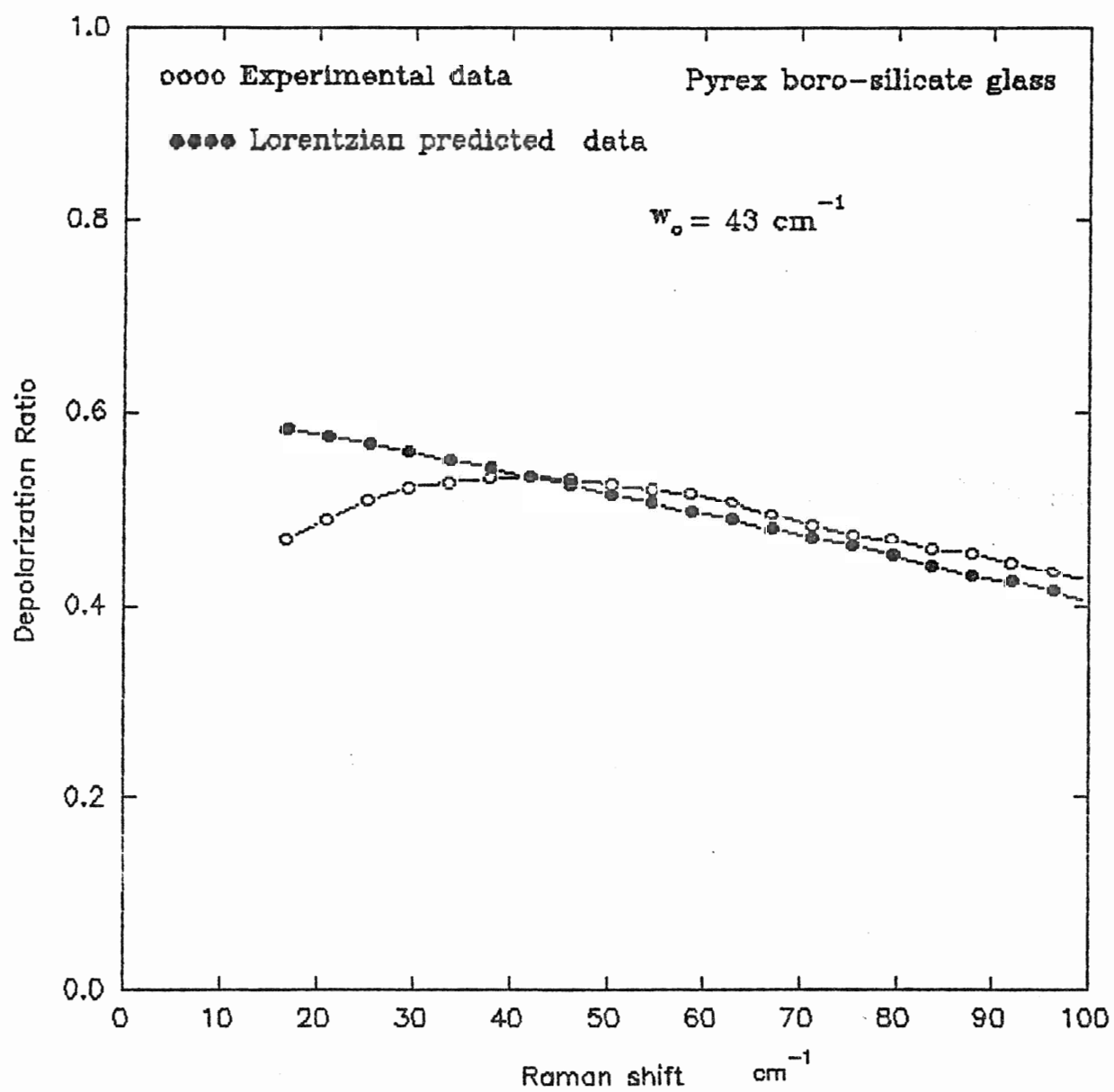


Fig. 4.13 Pyrex experimental and Lorentzian predicted depolarization ratio spectrum vs Raman shift (cm^{-1}).



ii) Fused quartz:

Fig. 4.14 shows the smoothed VV and VH Stokes spectra which were obtained at room temperature for fused quartz. The broad bands below 200 cm^{-1} are the result of a one-phonon process as shown by the same argument discussed earlier for pyrex glass. Fig. 4.14 shows an intense continuum extending from the exciting line to about 600 cm^{-1} . The continuum is characterized by two broad intensity maxima at 54 cm^{-1} and 430 cm^{-1} with a sharper peak at 480 cm^{-1} and a sharp intensity cut off at about 550 cm^{-1} . Fig. 4.14 also shows that the depolarization varies across the band. At the low-frequency end of the band the depolarization increases to reach a maximum depolarization ratio of 0.40 at $\omega = 54\text{ cm}^{-1}$, which is consistent with other findings (G.Winterling, 1975). For $\omega > 54\text{ cm}^{-1}$, ρ starts to decrease and has the values of 0.04 at the second peak ($\omega = 430\text{ cm}^{-1}$) and 0.02 at the sharper peak ($\omega = 480\text{ cm}^{-1}$). Fig. 4.15 shows the reduced VV and VH spectra for fused quartz.

The fit of the theoretical VH spectrum based on the Gaussian correlation function, Eq (4), to the experimental values for quartz is shown in Fig. 4.16 for $\omega = 20$ to 300 cm^{-1} , where the values $v_t = (3.75 \times 10^5\text{ cm / s})$ and $v_L = (5.94 \times 10^5\text{ cm / s})$ are obtained from Brillouin scattering (Shapiro et al, 1966). The fit for $\omega \leq 50\text{ cm}^{-1}$ is good but a strong deviation from the experimental data is observed at $\omega > 50\text{ cm}^{-1}$. The obtained value of σ to fit the experimental and predicted values at the top of the LFB peak was $4.5 \times 10^{-8}\text{ cm}$. According to the criterion of the long-wave limit, the deviation occurs where the MB theory no longer applies ($\omega > 44\text{ cm}^{-1}$). The theoretical value of σ is estimated from Eq (16), where $v = v_t$ because for the VH scattering the intensity is mostly

contributed by the transverse acoustic modes. The expected and experimental values of $\sigma = 4.0 \times 10^{-8}$ cm and $\sigma = 4.5 \times 10^{-8}$ cm respectively agree within experimental error.

Fig. 4.17 shows the fit of Eq (5) to the experimental VV spectrum, where the quantity M is measured from the experimental depolarization. A good fit is obtained for $\omega \leq 50 \text{ cm}^{-1}$ but there is a strong deviation from the experimental results for $\omega > 50 \text{ cm}^{-1}$. The contributions from vibrational modes that are not describable by an elastic model because of the frequency limitations of the MB theory may be responsible for this deviation. As for the VH spectrum, the value of $\sigma = 4.5 \times 10^{-8}$ cm gives a fit of the theory to the experiment at the top of the LFB peak. The predicted value of σ from Eq (16), where v is the average of the longitudinal and transverse velocities of the acoustic waves, is 5.1×10^{-8} cm. Fig. 4.18 shows the fit of Eq 8 to the experimental ρ . The figure shows that the theory fits neither the shape nor the values of the experimental ρ . The value of $M = 0.1$ fitted both ρ and VV to Eqs (8) and (5) respectively at the peak of the LFB.

The predictions for the VH, VV, and depolarization spectra based on the Poisson correlation function are shown in Figs 4.19 - 4.21. Fig. 4.19 shows the fit of Eq (10) to the VH experimental spectrum. The value of $\omega_0 = 50 \text{ cm}^{-1}$ was found to fit the predicted spectrum to the experimental values at the peak of the LFB. Fig. 4.19 shows a good fit throughout the region of interest (20 to 100 cm^{-1}) which extends to about 200 cm^{-1} . From Eq (9b), where $v = 3.75 \times 10^5 \text{ cm / s}$ and $\omega_0 = 50 \text{ cm}^{-1}$, the structural correlation radius was calculated to be 8.0×10^{-8} cm.

Fig. 4.20 shows the fit of the predicted VV spectrum to the experimental values, where the quantity M in the fitting equation was measured from the experimental depolarization. The good fit in Fig. 4.20 covers the entire region of interest. As for the VH spectrum, the value of $\omega_0 = 50 \text{ cm}^{-1}$ was required to get the best fit of the theory to the experimental data at the peak of the LFB. Fig. 4.21 shows the fit of Eq (8a), with (g_t / g_L) given by Eq (11b), to the experimentally obtained depolarization. The figure also shows that the equation neither fits the shape nor the values of the experimental depolarization spectrum. There is a maximum difference of about 30% between their values in the region $\omega < 50 \text{ cm}^{-1}$ and a maximum difference of 12% in the region (50 to 100 cm^{-1}). The quantity $M = 3.55$ fitted both ρ and the VV spectra to their experimental counterparts at the top of the LFB peak. The quantity M provides a much better fit for the VV spectrum for the rest of the region because the VV spectrum is not very sensitive to it.

The results for the VH, VV, and ρ spectra based on the MB theory with a Lorentzian correlation function are also applied to our experimental data. Fig. 4.22 shows the fit of Eq (14), with $\omega_0 = 50 \text{ cm}^{-1}$ and the $\text{SCR} = 6.2 \times 10^{-8} \text{ cm}$, to the experimental VH spectrum. The figure shows a good fit in the region $50 \leq \omega \leq 200 \text{ cm}^{-1}$ but there is a deviation in the fit for $\omega < 50 \text{ cm}^{-1}$. Fig. 4.23 shows the fit of Eq (13) to the experimentally obtained VV spectrum. As for the VH spectrum the value of $\omega_0 = 50 \text{ cm}^{-1}$ was required to achieve the agreement between the two at the top of the LFB peak. The figure shows a good fit in the region $50 \leq \omega \leq 150 \text{ cm}^{-1}$ but the fit is poor for $\omega < 50 \text{ cm}^{-1}$. Fig. 4.24 shows the fit of Eq (8), with (g_t / g_L) given by Eq (15), to the experimental

depolarization ratio. The value of $M = 0.36$ in Eq (8) provided the agreement between the VV and ρ to their experimental counterparts at the peak of the LFB . The predicted values of ρ are within 20% of the experimental values for $\omega < 50 \text{ cm}^{-1}$ but there is a maximum difference of only about 5% in the region $50 \leq \omega \leq 150 \text{ cm}^{-1}$.

Fig. 4.14 Quartz VV and VH experimental intensity (arb. units) vs Raman shift (cm^{-1}).

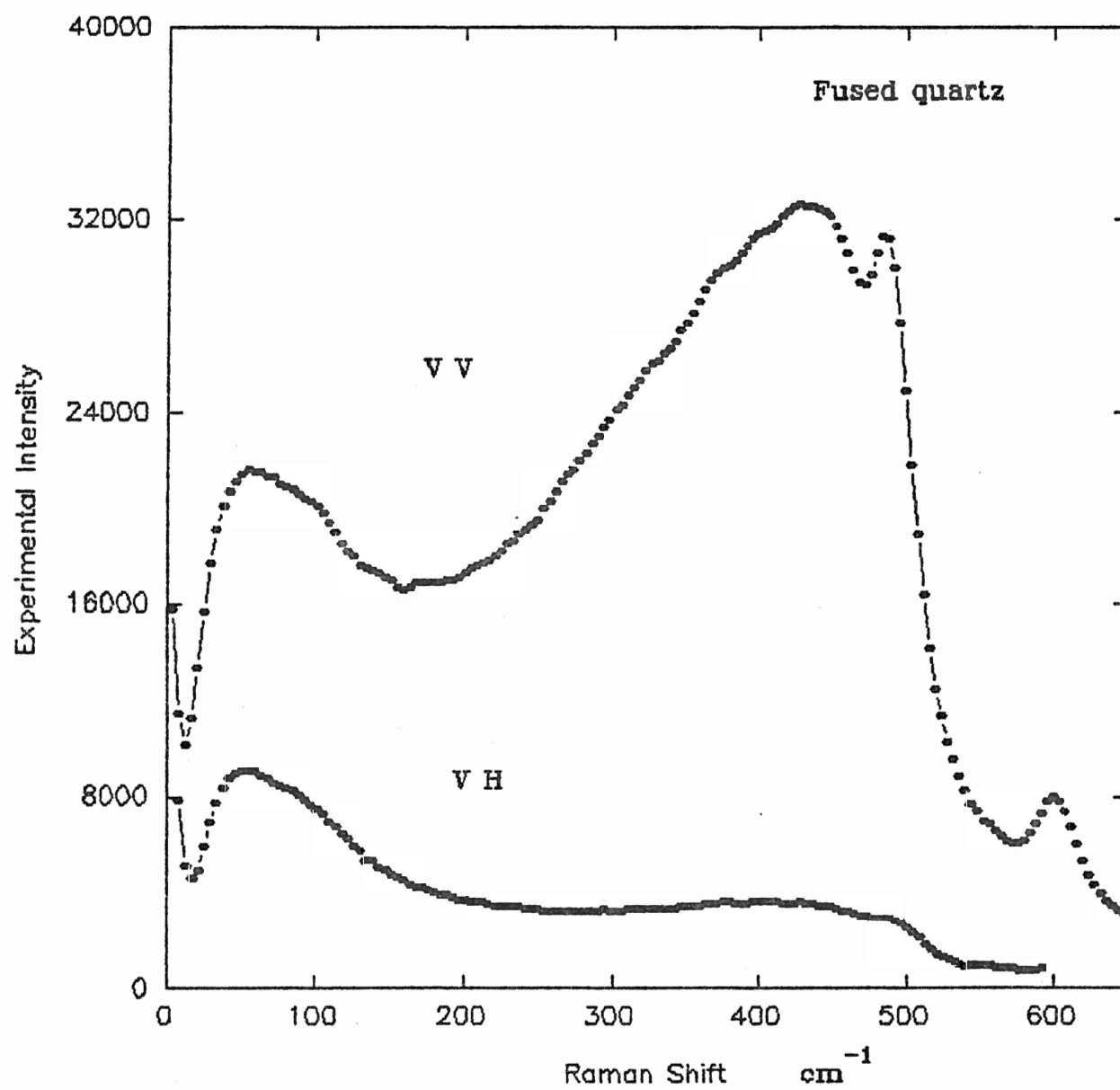


Fig. 4.15 Quartz experimental VV and VH reduced spectra
(arb. units) vs Raman shift (cm^{-1}).

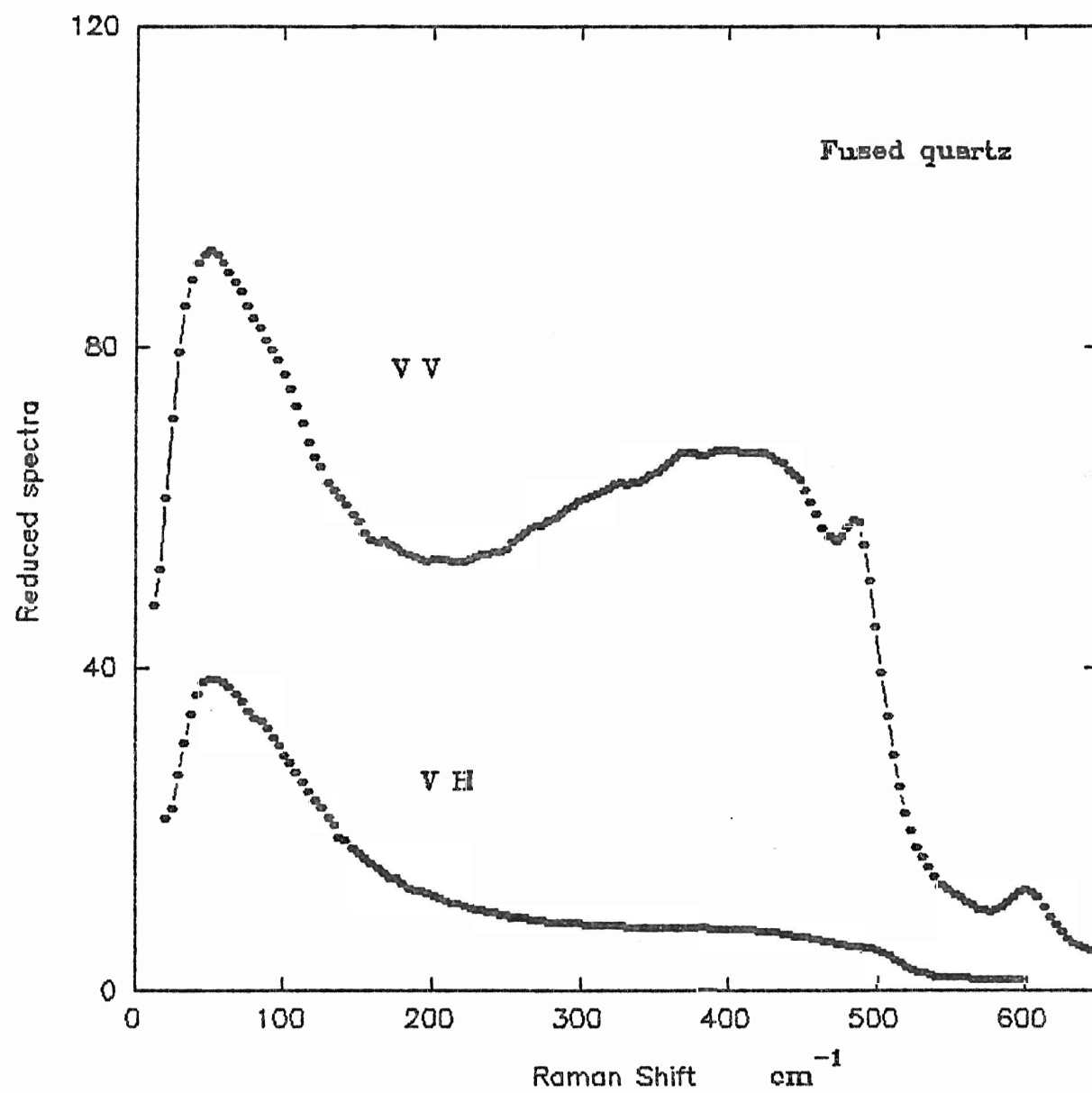


Fig. 4.16 Quartz experimental and Gaussian predicted VH reduced spectrum (arb. units) vs Raman shift (cm^{-1}).

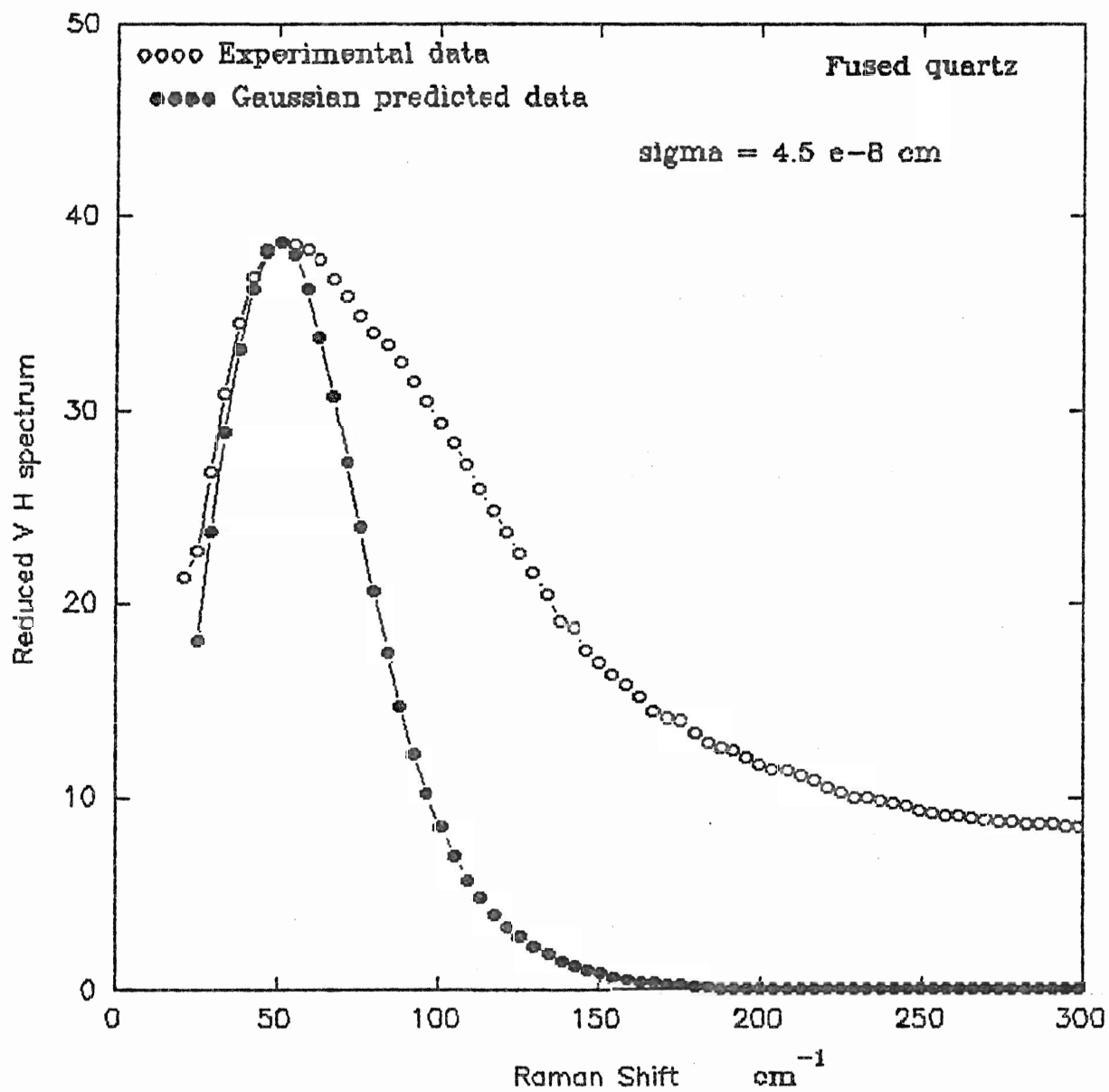


Fig. 4.17 Quartz experimental and Gaussian predicted VV reduced spectrum (arb.units) vs Raman shift (cm^{-1}).

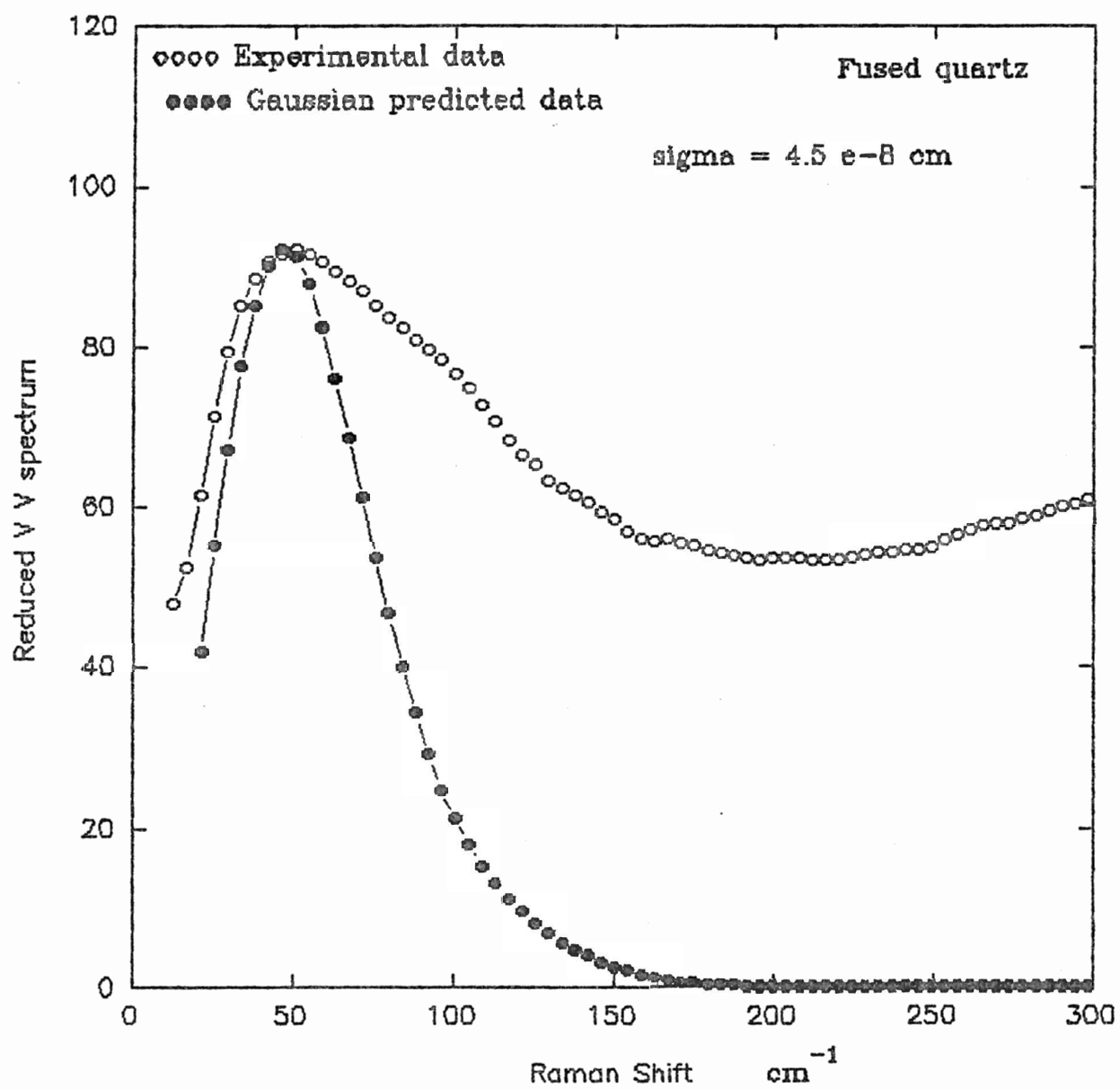


Fig. 4.18 Quartz experimental and Gaussain predicted depolarization ratio spectrum vs Raman shift (cm^{-1}).

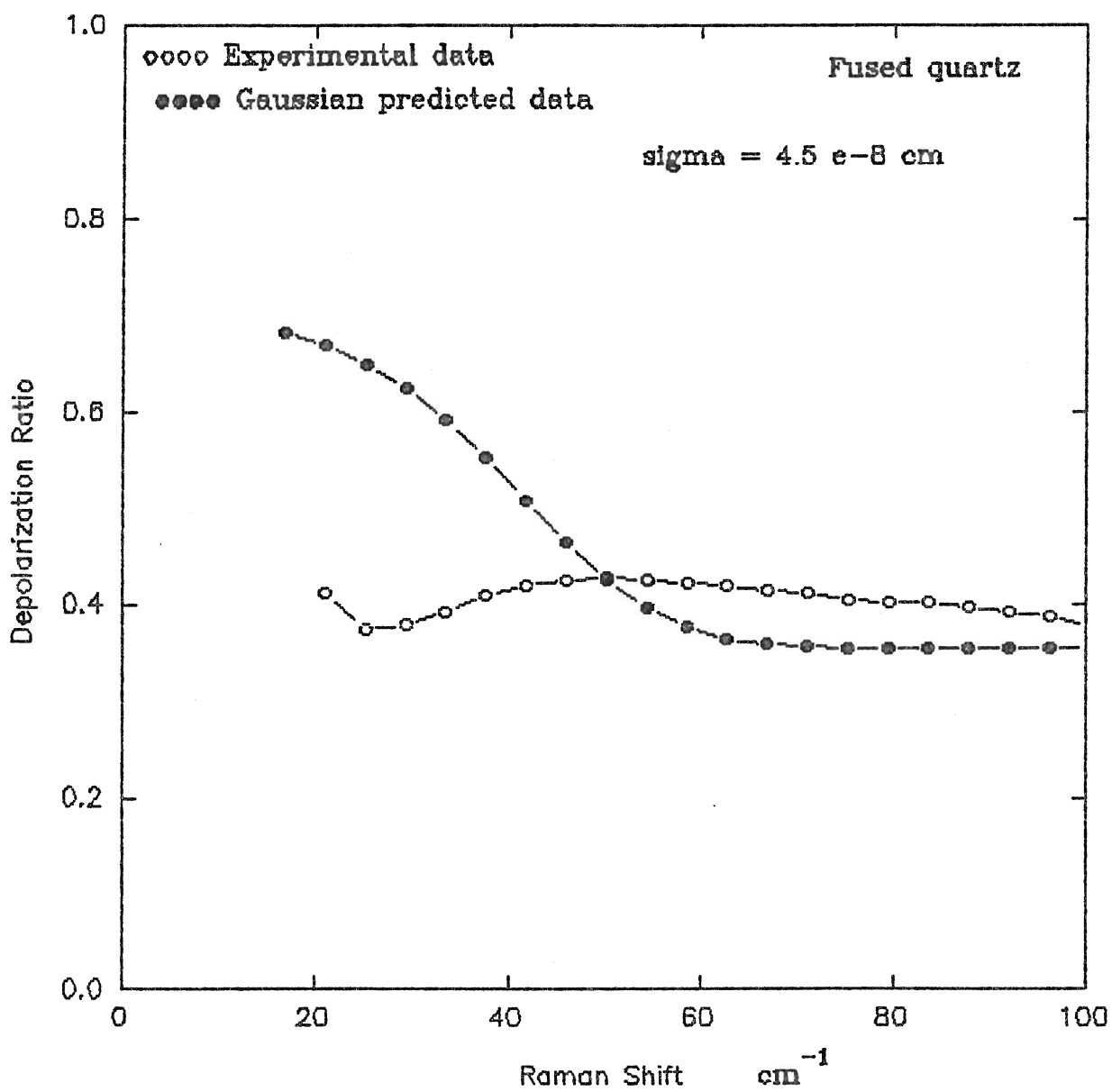


Fig. 4.19 Quartz experimental and Poisson predicted VH reduced spectrum (arb. units) vs Raman shift (cm^{-1}).

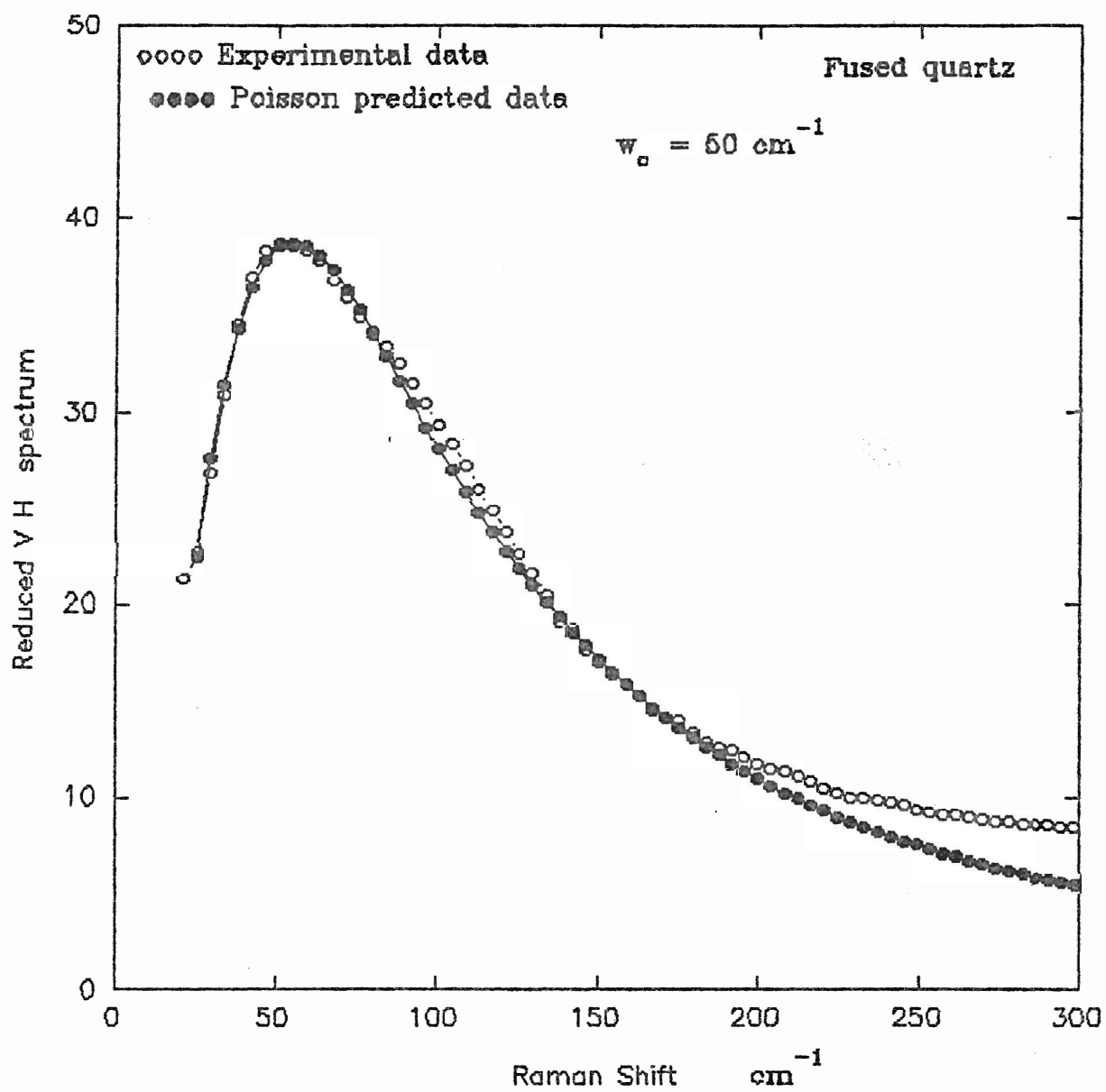


Fig. 4.20 Quartz experimental and Poisson predicted VV reduced spectrum (arb. units) vs Raman shift (cm^{-1}).

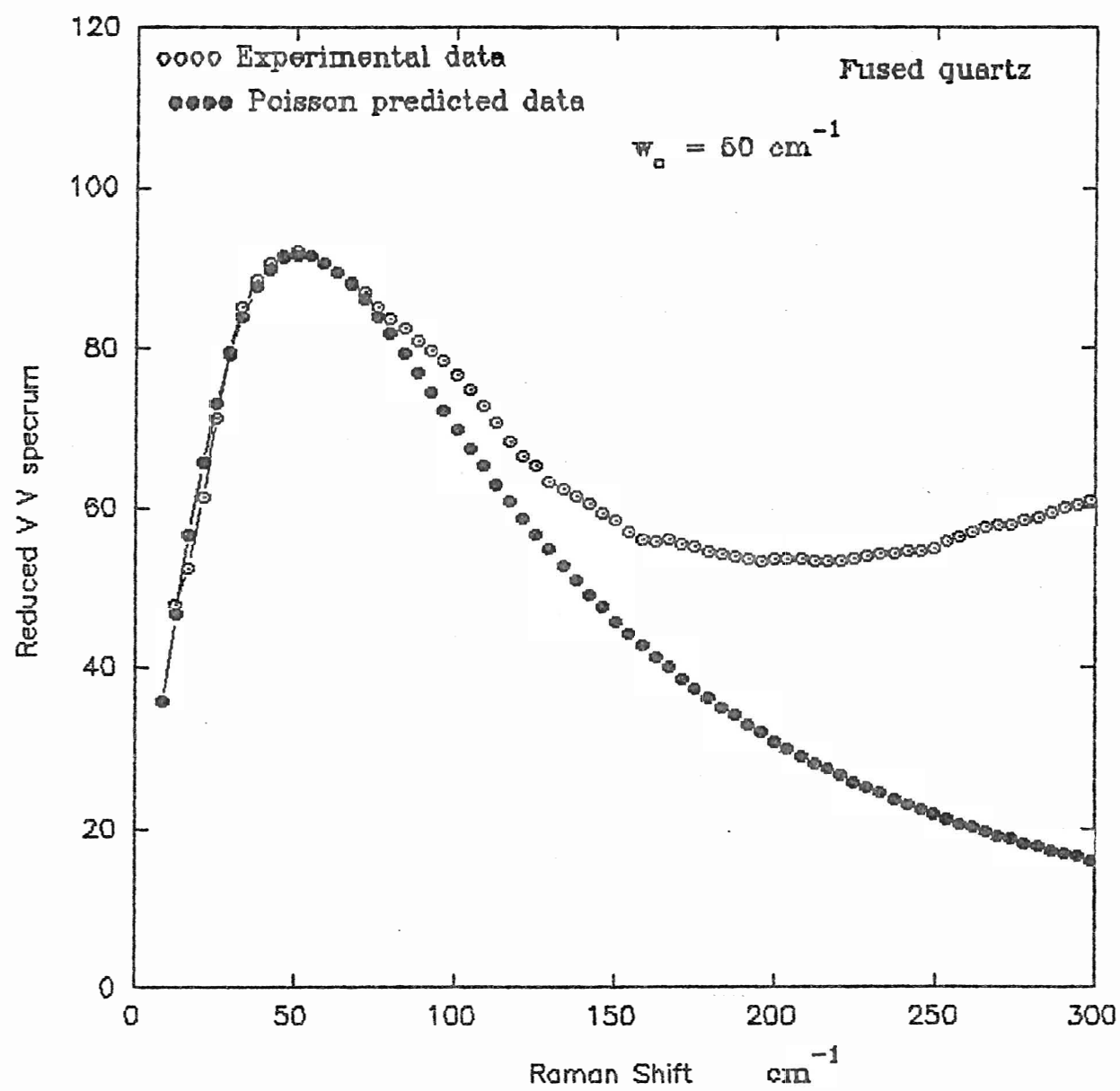


Fig. 4.21 Quartz experimental and Poisson predicted depolarization ratio spectrum vs Raman shift (cm^{-1}).

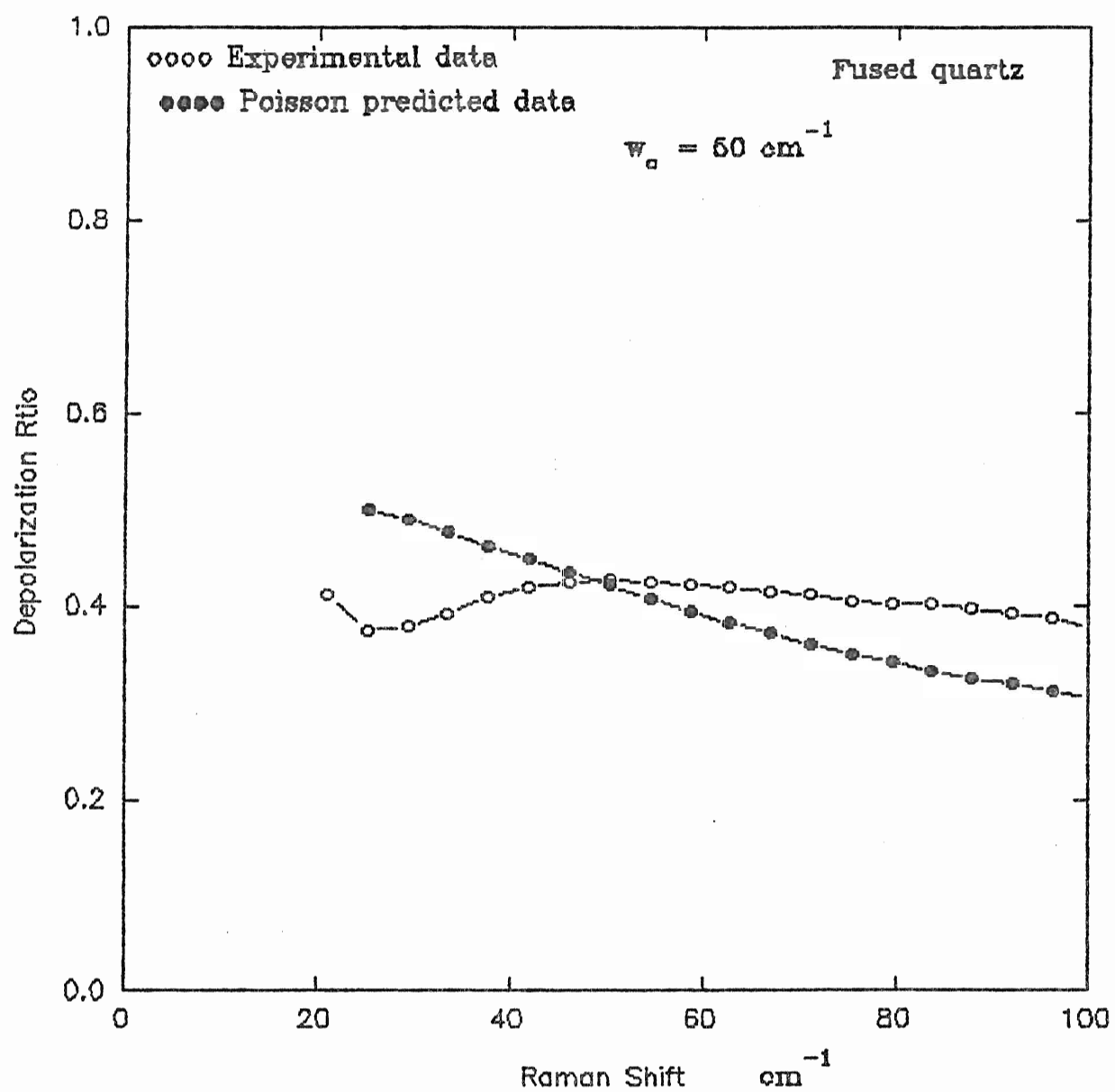


Fig. 4.22 Quartz experimental and Lorentzian predicted VH reduced spectrum (arb. units) vs Raman shift (cm^{-1}).

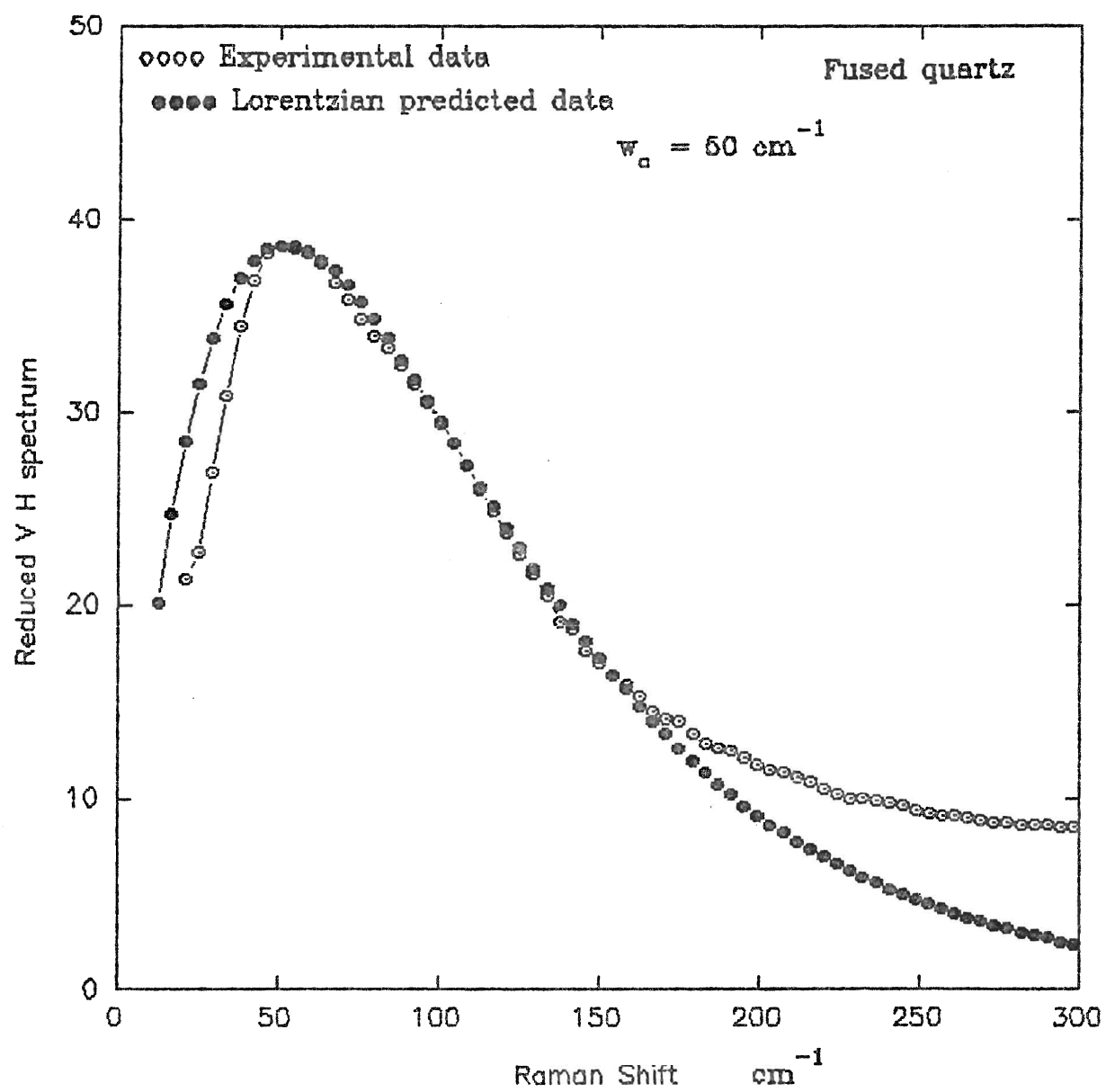


Fig. 4.23 Quartz experimental and Lorentzian predicted VV reduced spectrum (arb. units) vs Raman shift (cm^{-1}).

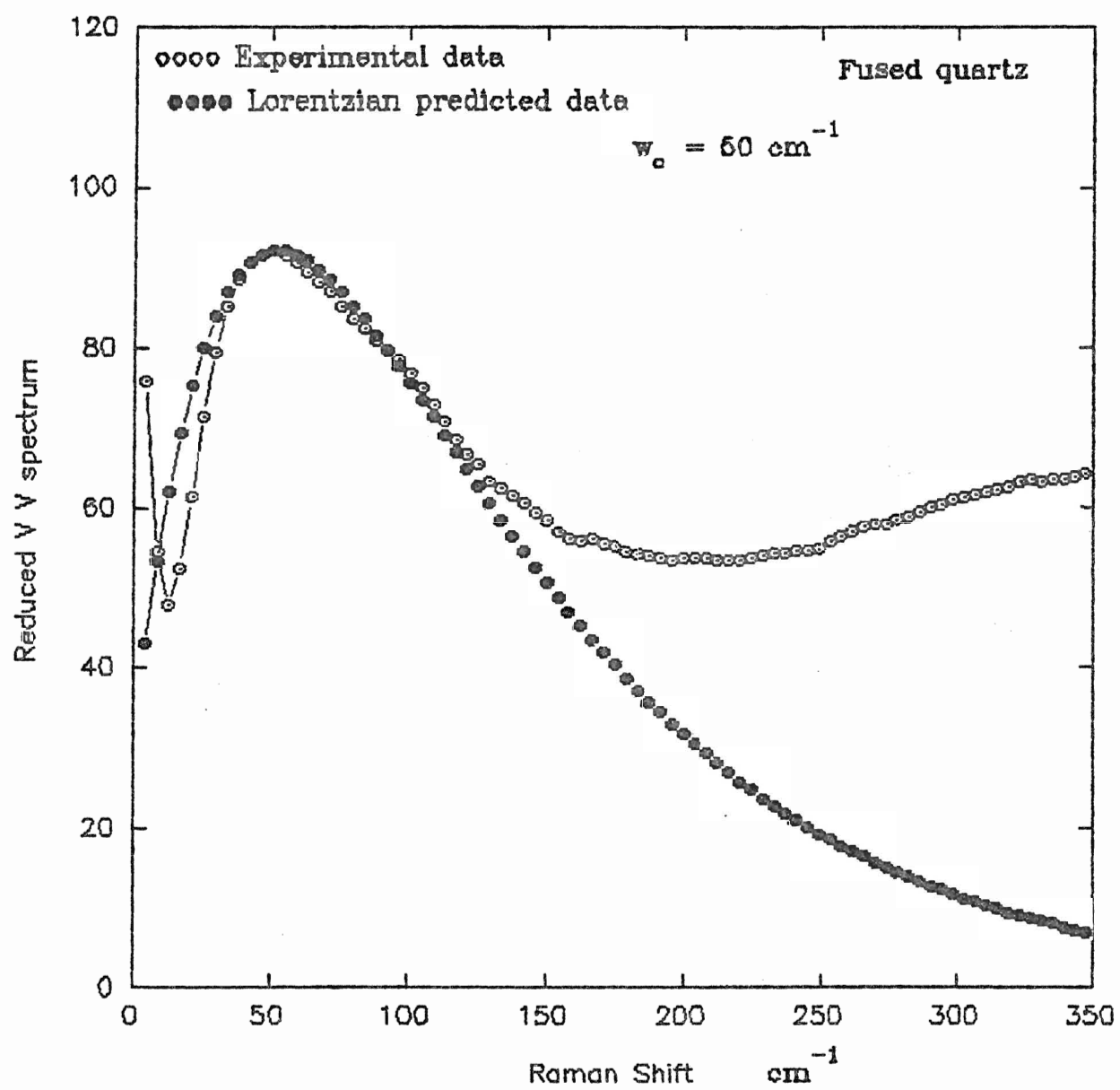
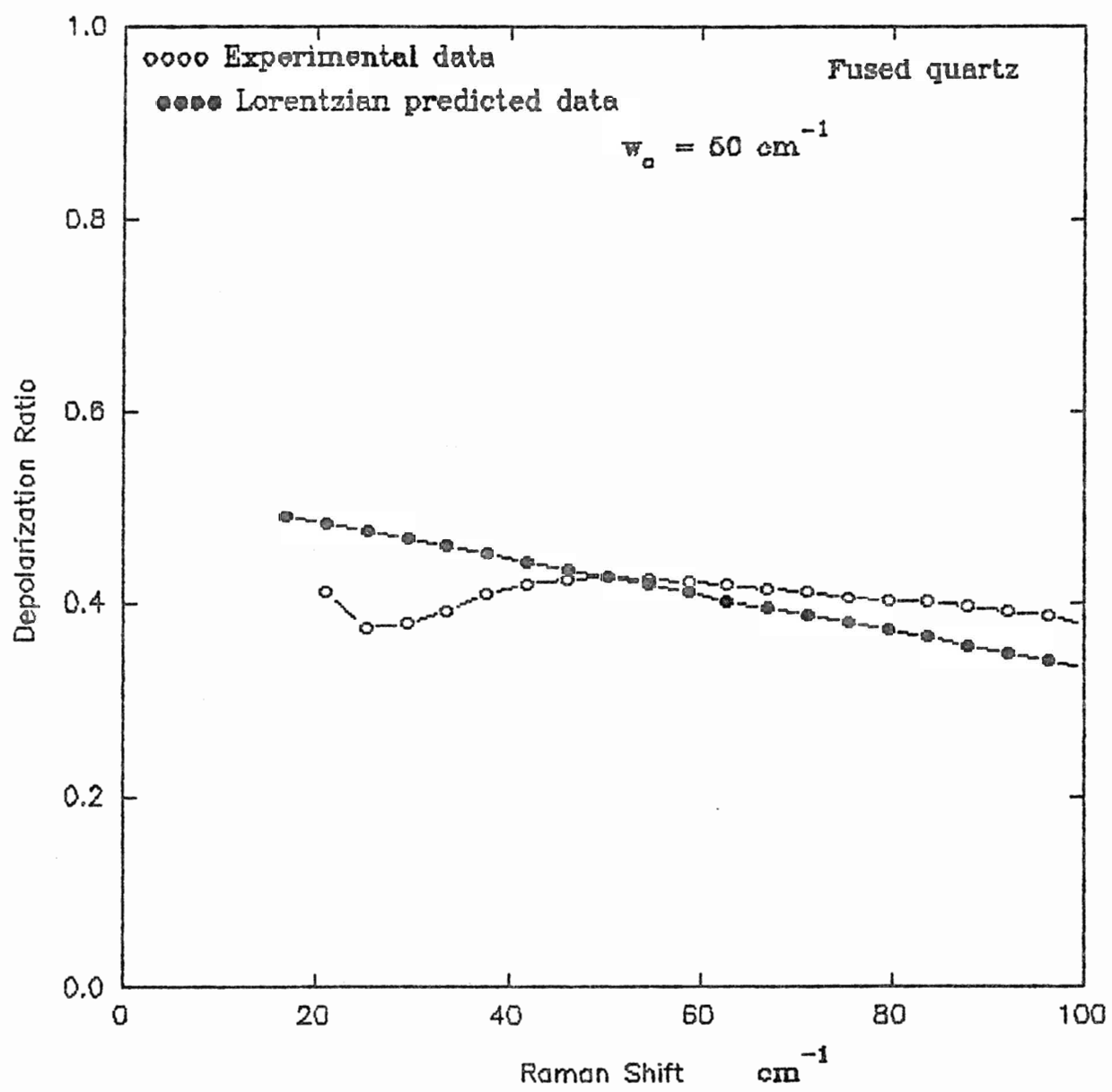


Fig. 4.24 Quartz experimental and Lorentzian predicted depolarization ratio spectrum vs Raman shift (cm^{-1}).



3) Soda-lime silicate glass:

Fig. 4.25 shows the smoothed VV and VH Stokes spectra which were obtained at room temperature and Fig. 4.26 shows the reduced spectra for the soda-lime silicate glass. Fig. 4.25 shows an intense continuum extending from the exciting line to about 800 cm^{-1} . The continuum is characterized by two broad intensity maxima at 70 cm^{-1} and 610 cm^{-1} at which the depolarization ratios are 0.38 and 0.35 respectively.

The fit of Eq (4) for the Gaussian function to the experimental VH spectrum is shown in Fig. 4.27 for $\omega = 20$ to 250 cm^{-1} , where $v_t = 2.94 \times 10^5 \text{ cm/s}$ and $v_L = 5.0 \times 10^5 \text{ cm/s}$. The value of 2σ required to fit the predicted and the experimental values at the maximum of the LFB was $6.0 \times 10^{-8} \text{ cm}$. The structural correlation radius (2σ) was theoretically estimated by Eq (16), with $v = v_t$, to be $8.7 \times 10^{-8} \text{ cm}$. Fig. 4.27 shows that the theory provides a poor fit to the experimental values in the region of interest (20 to 100 cm^{-1}). Fig. 4.28 shows the fit of Eq (5) to the experimental VV spectrum, where the quantity M in Eq (5) is measured from the experimentally obtained depolarization ratio. There is a reasonable fit for $\omega \leq 60 \text{ cm}^{-1}$ but a strong deviation from the experimental results is obvious for $\omega > 60 \text{ cm}^{-1}$. As for the VH spectrum, the value of $(2\sigma) = 6.0 \times 10^{-8} \text{ cm}$ fitted the experimental and the predicted VV spectrum at the peak of the LFB. From Eq (16) where v is the average of v_t and v_L , 2σ is estimated to be $7.0 \times 10^{-8} \text{ cm}$. Fig. 4.29 shows the fit of Eq (8) to the experimental ρ . The figure shows that the theory provides a good fit for $\omega \geq 50 \text{ cm}^{-1}$ but the fit is poor for $\omega < 50 \text{ cm}^{-1}$. The value of $M = 0.85$ fitted both ρ and VV experimental spectra to Eqs (8) and (5) respectively at the top of LFB.

The fits for the VH, VV, and ρ spectra based on a Poisson correlation function to our experimental data are shown in Figs 4.30-4.32. Fig. 4.30 shows the fit of Eq (10) to the experimental VH spectrum. The value of $\omega_0 = 60 \text{ cm}^{-1}$ fitted the theory to the experimental spectrum at the top of the LFB. The figure shows a good fit only in the region $48 \leq \omega \leq 90 \text{ cm}^{-1}$. From Eq (9b), where $v = 2.94 \times 10^5 \text{ cm/s}$ and $\omega_0 = 60 \text{ cm}^{-1}$, the SCR was calculated to be $5.2 \times 10^{-8} \text{ cm}$. Fig. 4.31 shows the fit of Eq (11) to the experimental VV spectrum. The theory provides a good fit in the region $35 \leq \omega \leq 85 \text{ cm}^{-1}$. As for the VH spectrum, $\omega_0 = 60 \text{ cm}^{-1}$ gave the agreement between the predicted and the experimental values at the maximum of the LFB. Fig. 4.32 shows the fit of Eq (8a), with (g_t / g_L) given by Eq (11b), to the experimental ρ . The theory provides a fit with a maximum difference of about 10% for $\omega \leq 60 \text{ cm}^{-1}$ and about 25% for $\omega > 60 \text{ cm}^{-1}$. The quantity $M = 7.0$ fitted both ρ and VV spectra to their experimental values at the top of the LFB.

The results of the VH, VV, and ρ based on a Lorentzian correlation function are shown in Figs. 4.33-4.35. Fig. 4.33 shows the fit of Eq (14), with $\omega_0 = 60 \text{ cm}^{-1}$, to the experimental VH spectrum. The figure shows a good fit of the theory to the experimental data throughout the region of interest. Fig 4.34 shows the fit of Eq (13) to the experimental VV spectrum. As for the VH spectrum, the value of $\omega_0 = 60 \text{ cm}^{-1}$, so the $\text{SCR} = 6.2 \times 10^{-8} \text{ cm}$, provided the agreement between the theory and the experimental data at the peak of the LFB. Fig. 4.34 shows a good fit of the theory to the experimental results in the region of interest. Fig. 4.35 shows the fit of Eq (8a), with (g_t / g_L) given by Eq (15), to the experimental ρ . The figure shows a reasonable fit with a maximum

difference of about 5% for $\omega \leq 60 \text{ cm}^{-1}$ and 23% for $\omega > 60 \text{ cm}^{-1}$. The value of $M = 1.10$ was found to fit both VV and ρ spectra to their experimental counterparts at the peak of the LFB.

Fig. 4.25 Soft glass experimental VV and VH Intensity (arb. units)
vs Raman shift (cm^{-1}).

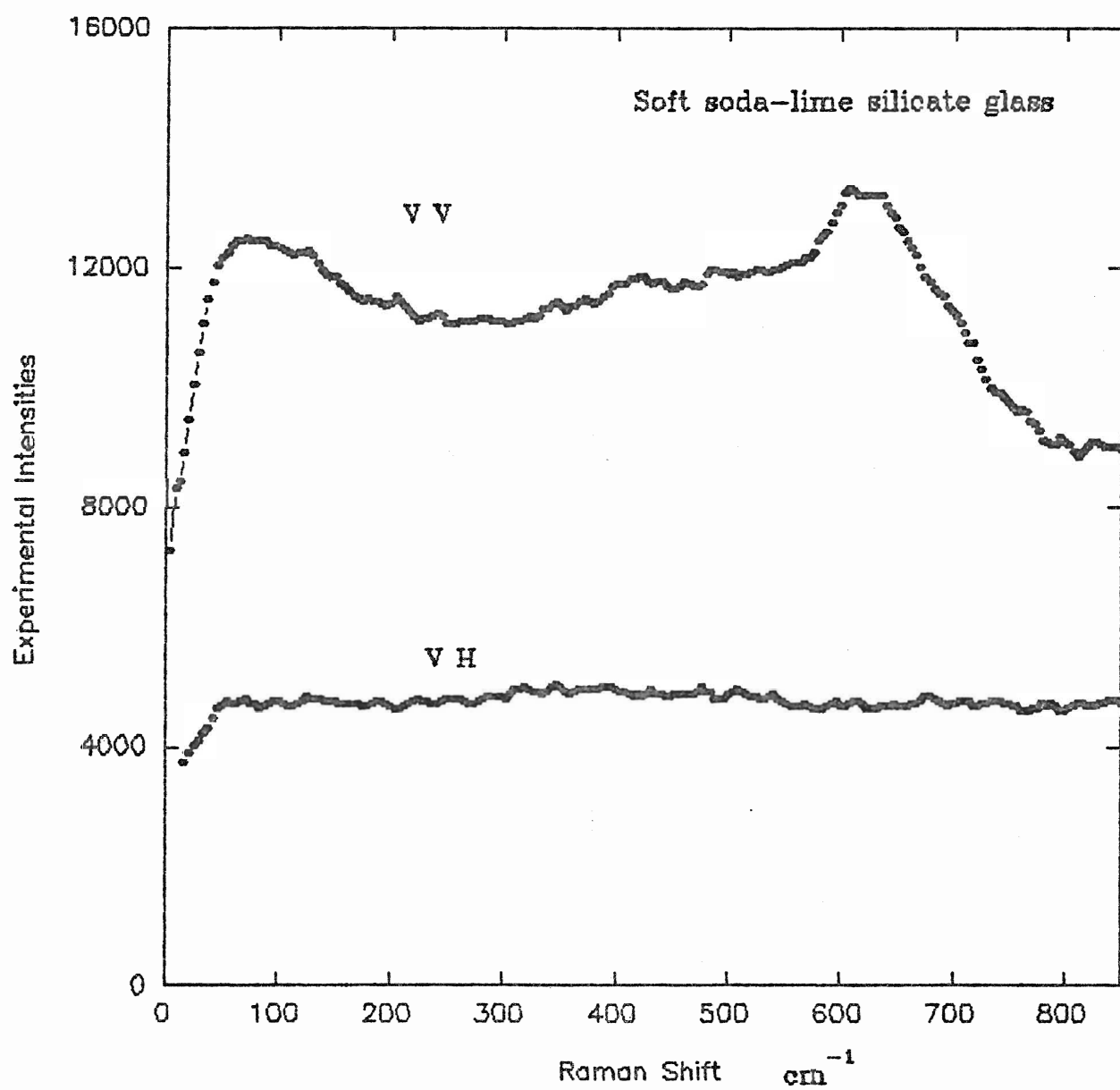


Fig. 4.26 Soft glass experimental VV and VH reduced spectra (arb. units) vs Raman shift (cm^{-1}).

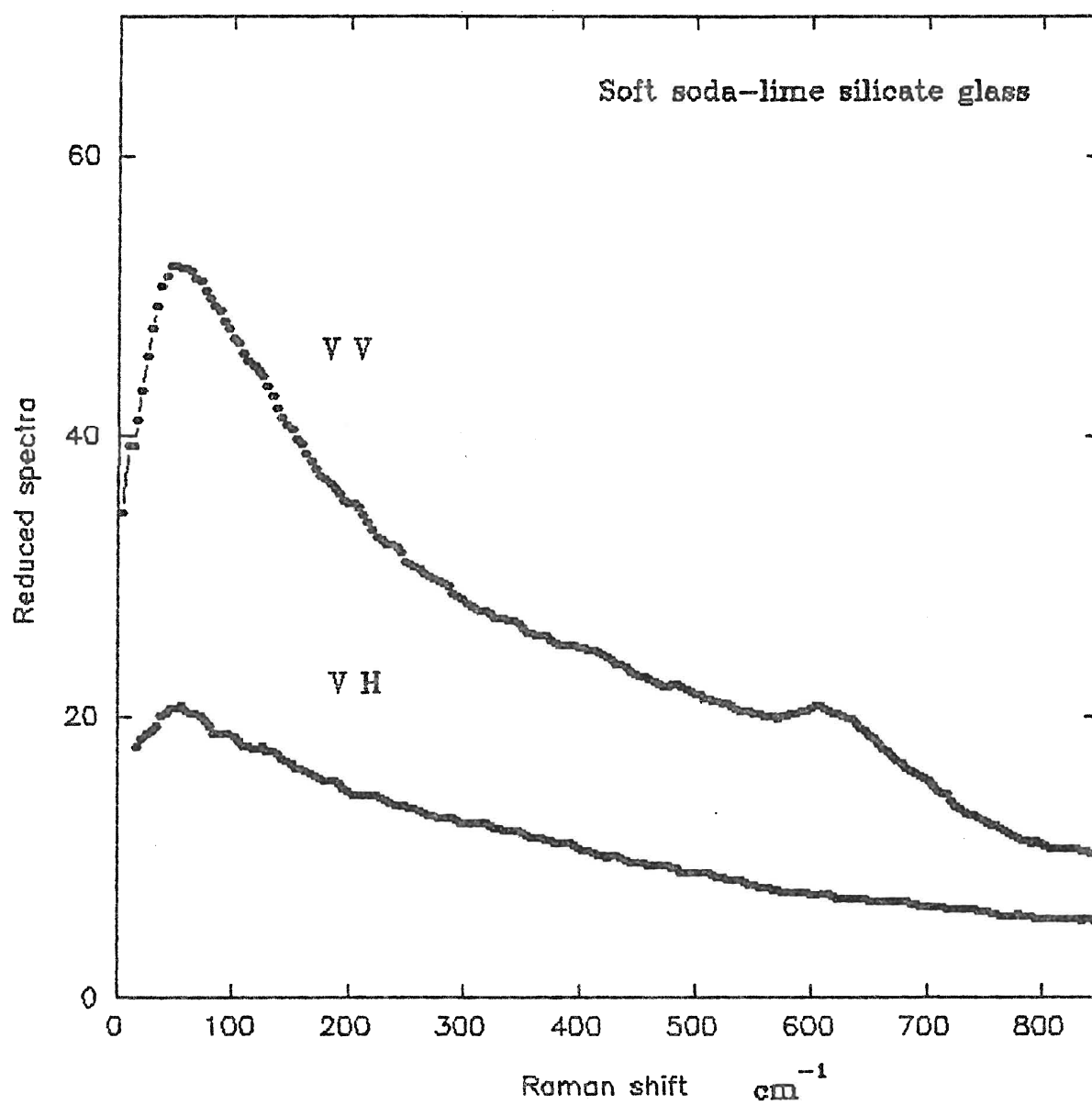


Fig. 4.27 Soft glass experimental and Gaussian predicted VH reduced spectrum (arb. units) vs Raman shift (cm^{-1}).

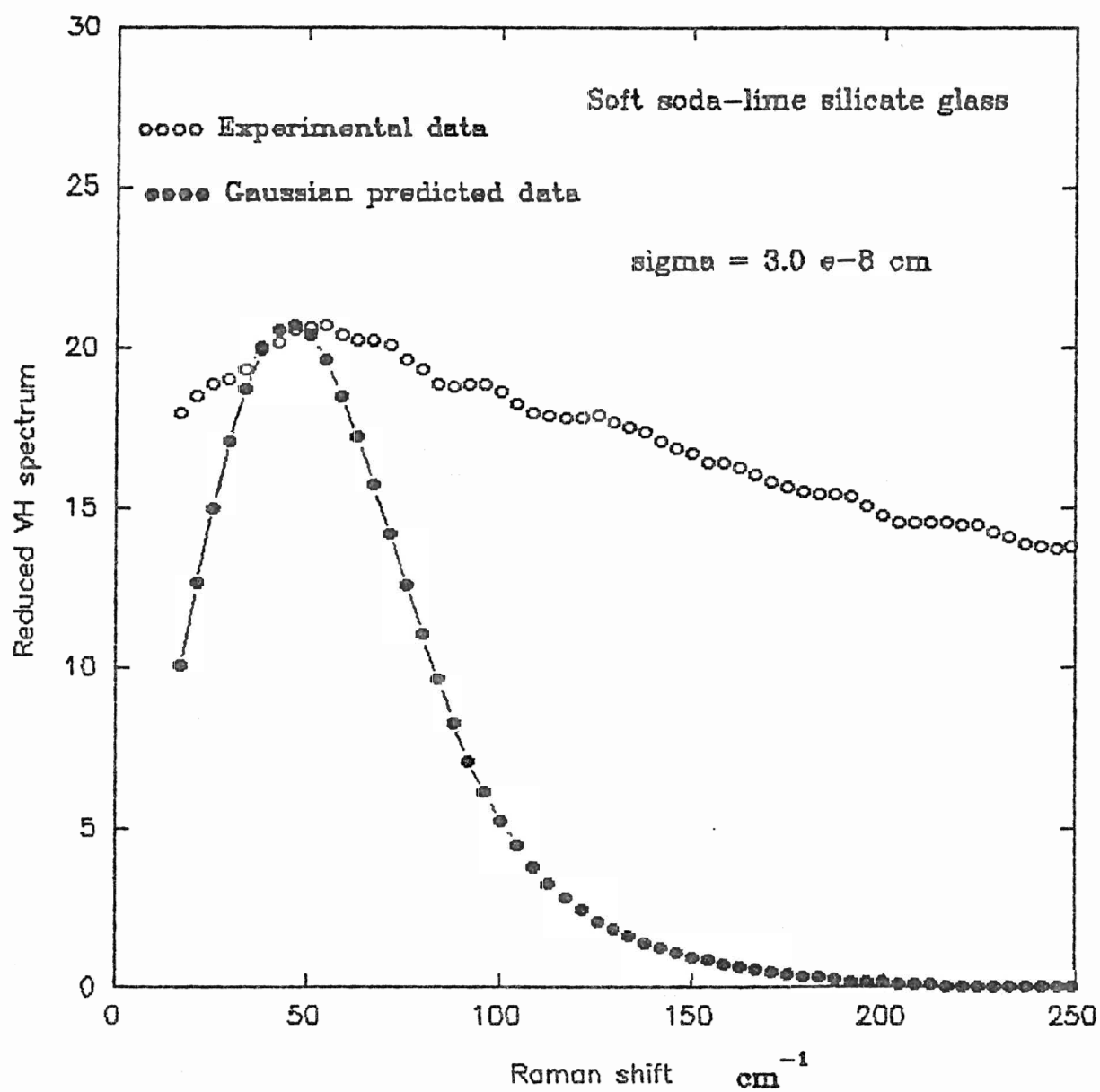


Fig. 4.28 Soft glass experimental and Gaussian predicted VV reduced spectrum (arb.units) vs Raman shift (cm^{-1}).

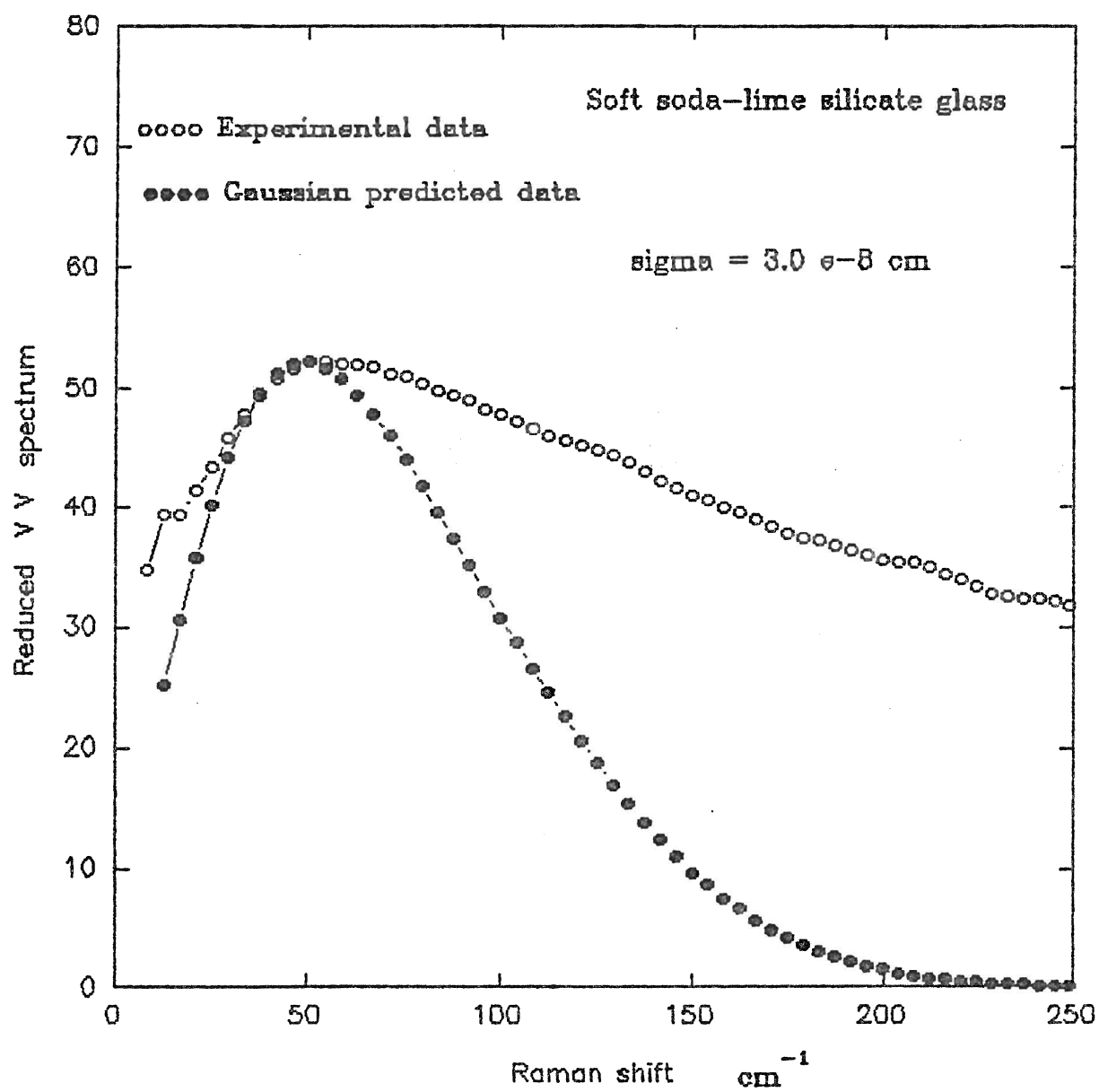


Fig. 4.29 Soft glass experimental and Gaussain predicted depolarization ratio spectrum vs Raman shift (cm^{-1}).

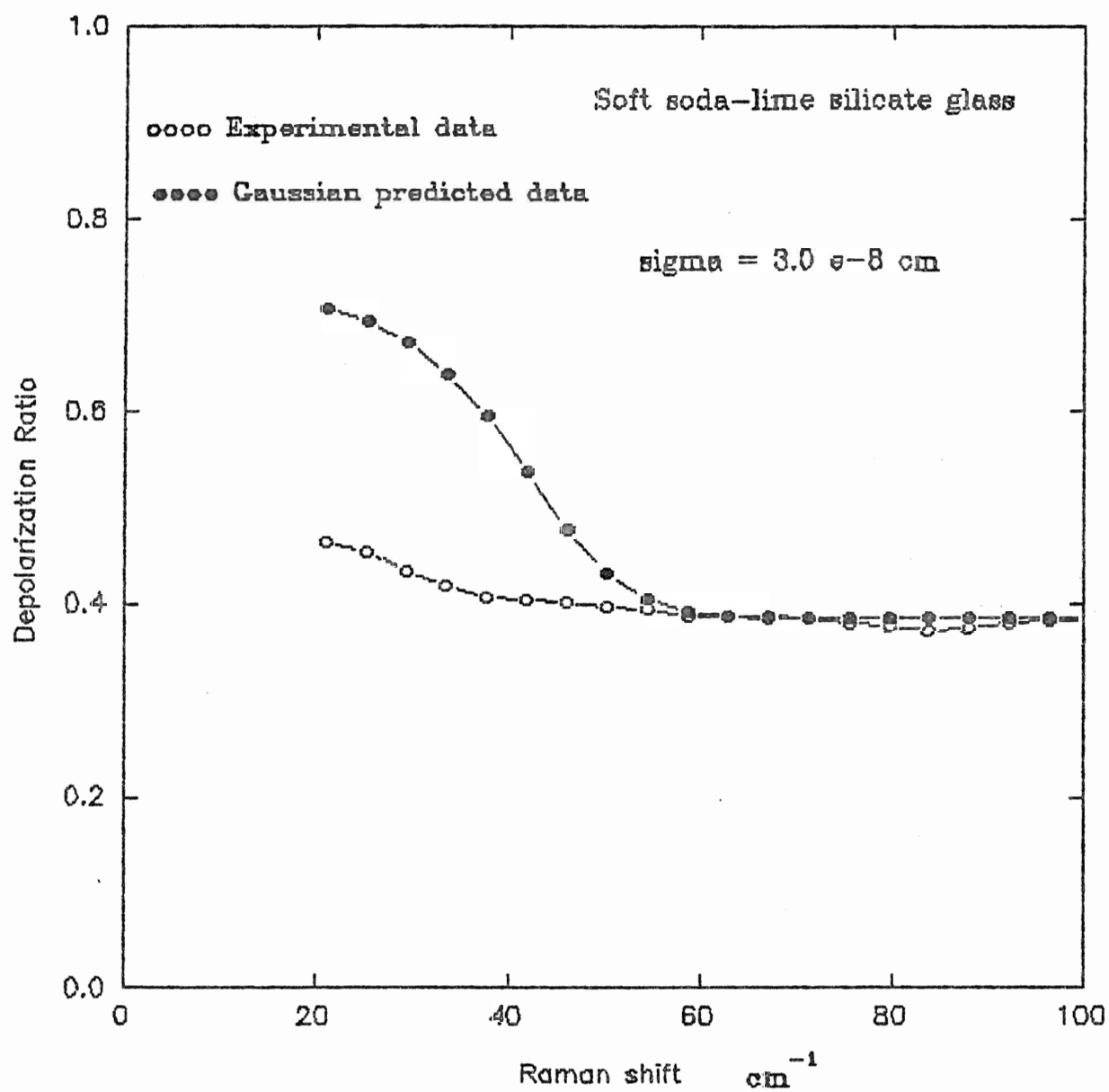


Fig. 4.30 Soft glass experimental and Poisson predicted VH reduced spectrum (arb. units) vs Raman shift (cm^{-1}).

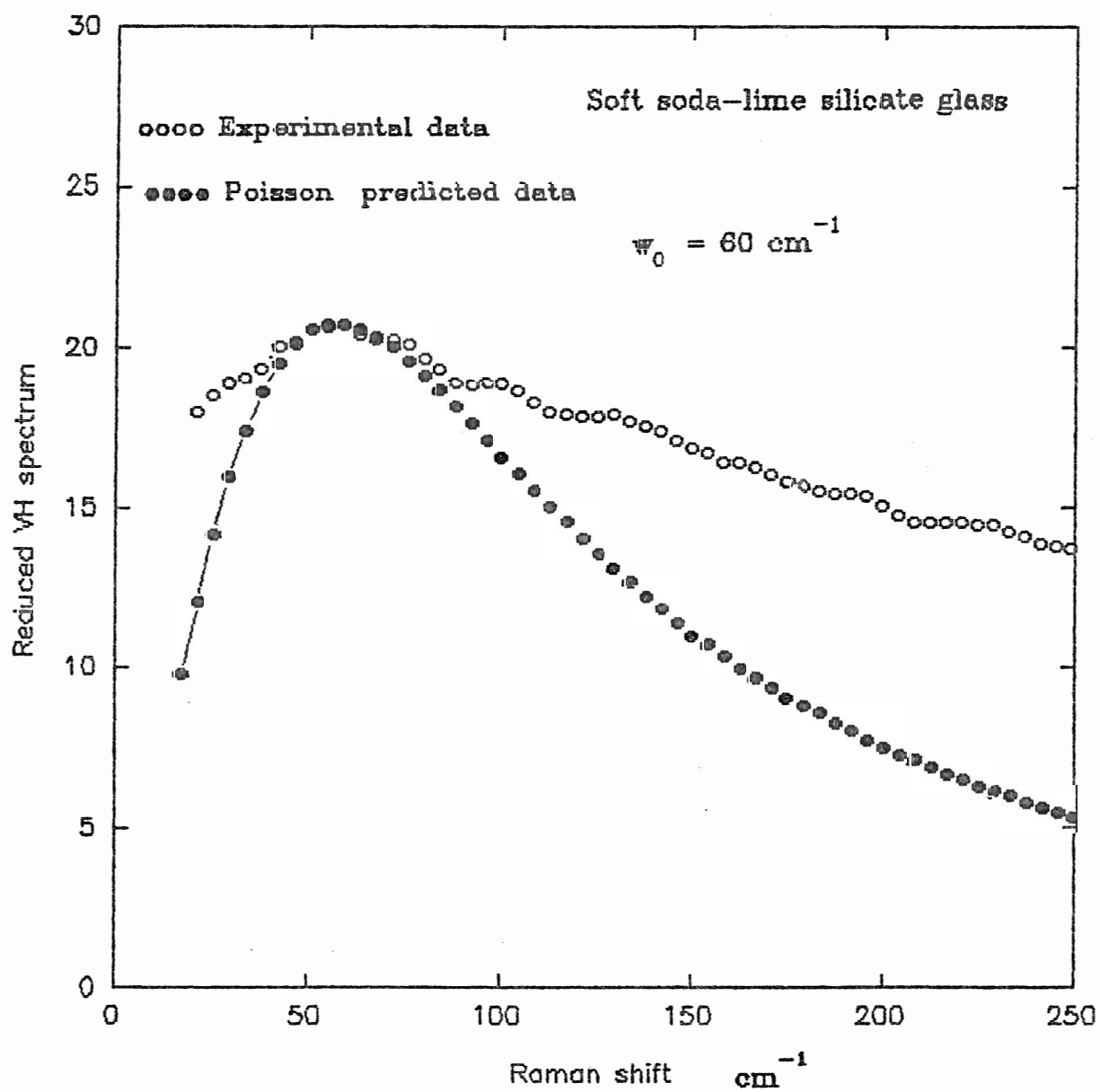


Fig. 4.31 Soft glass experimental and Poisson predicted VV reduced spectrum (arb. units) vs Raman shift (cm^{-1}).

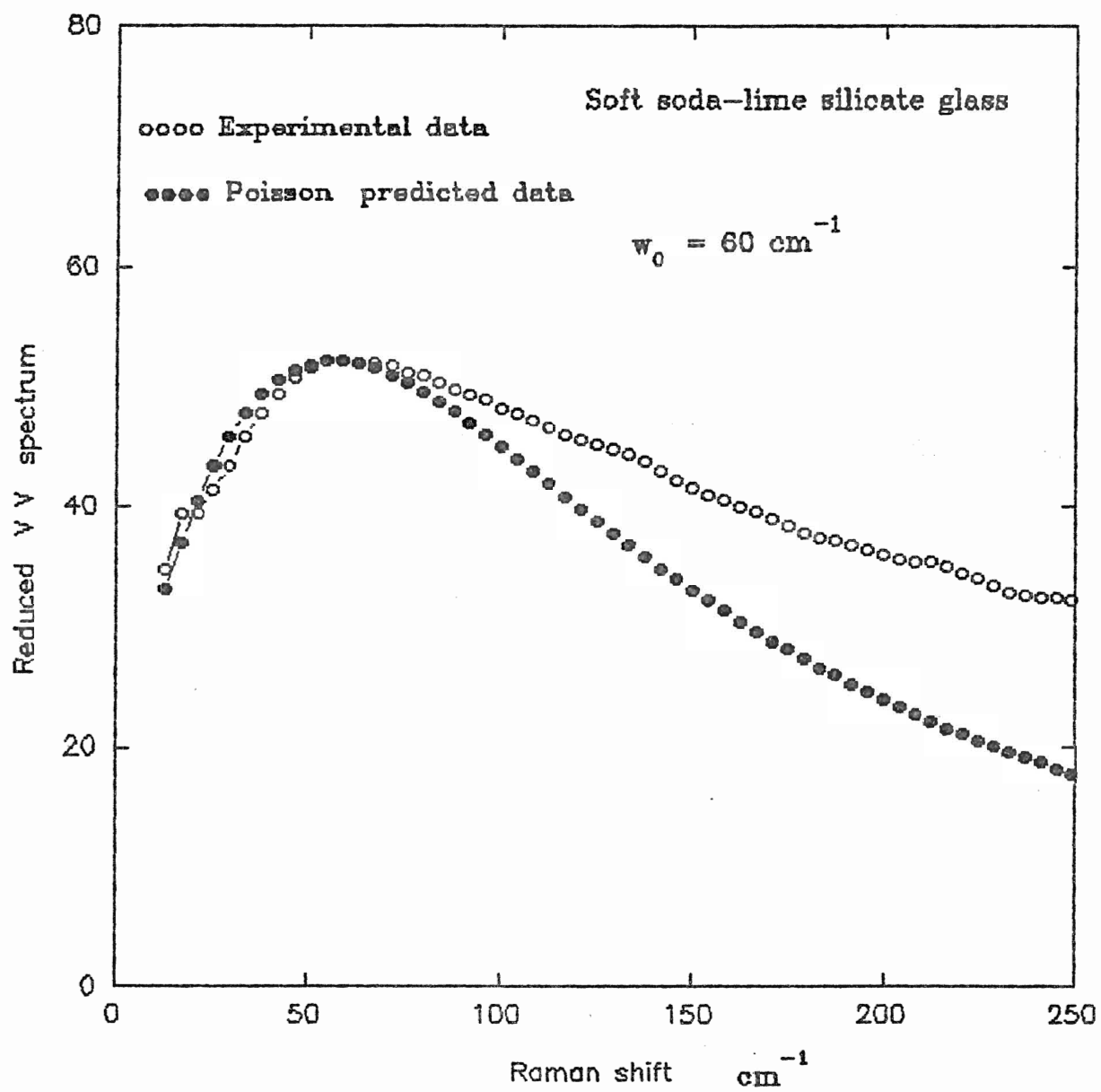


Fig. 4.32 Soft glass experimental and Poisson predicted depolarization ratio spectrum vs Raman shift (cm^{-1}).

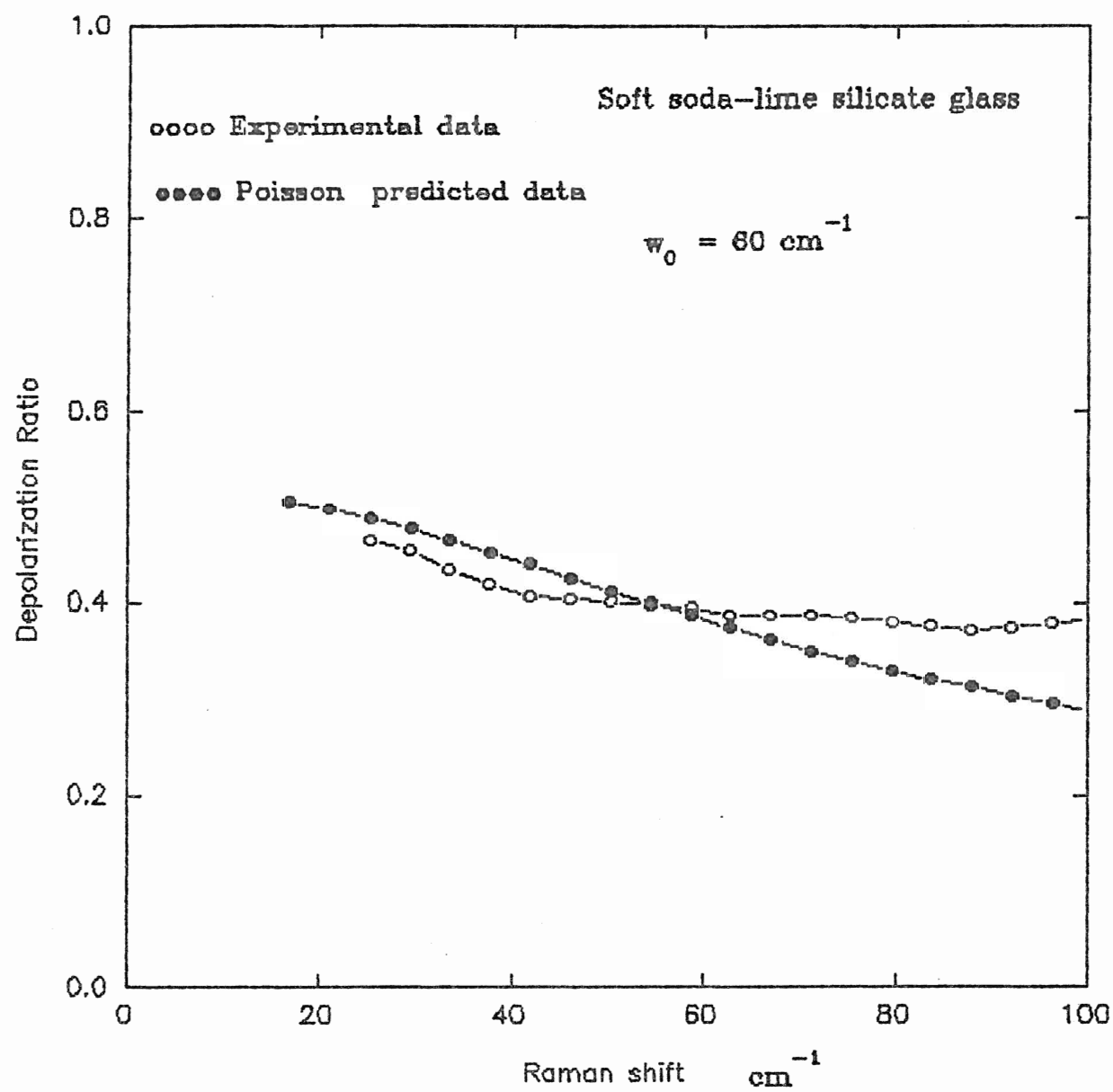


Fig. 4.33 Soft glass experimental and Lorentzian predicted VH reduced spectrum (arb. units) vs Raman shift (cm^{-1}).

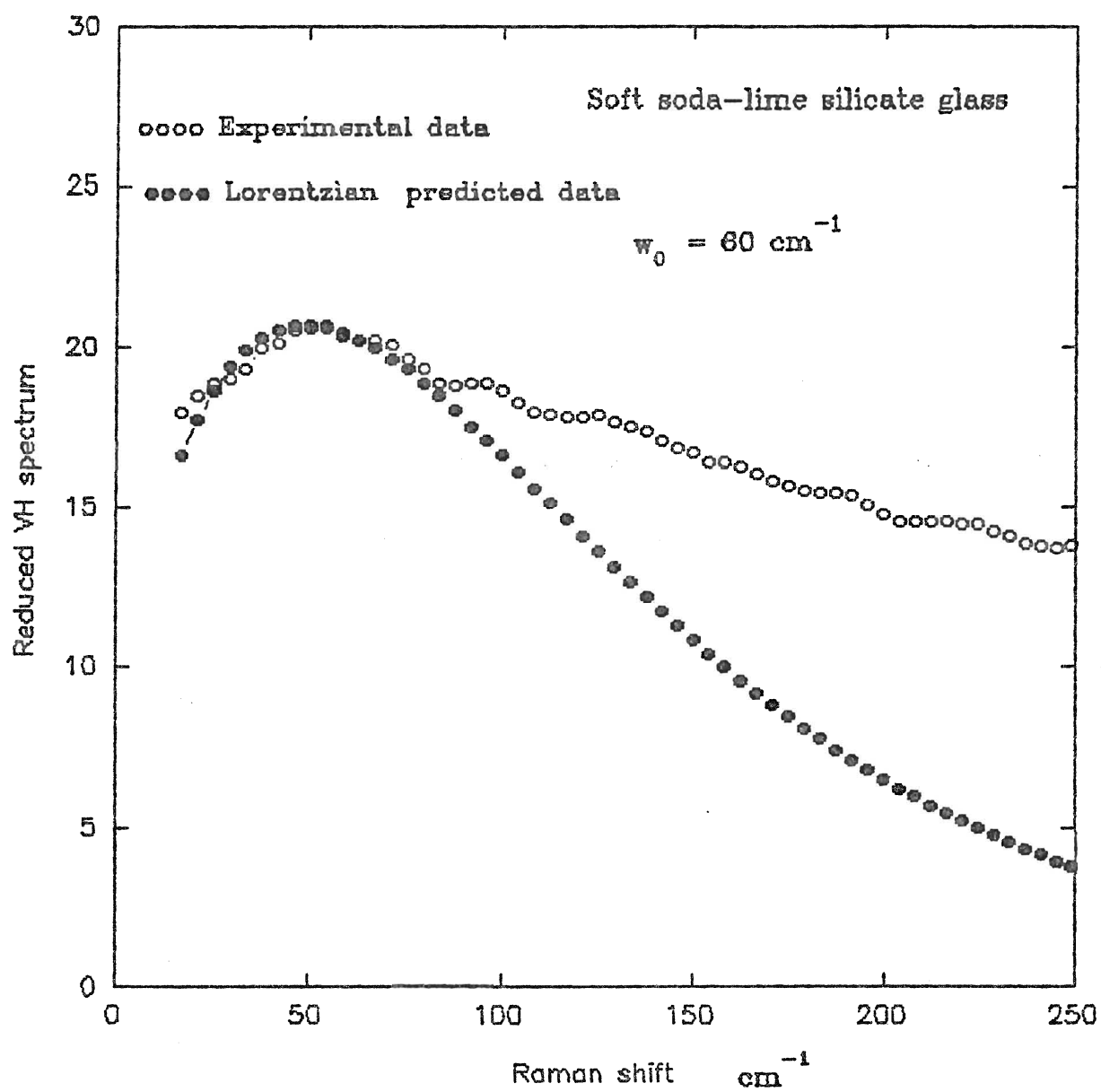


Fig. 4.34 Soft glass experimental and Lorentzian predicted VV reduced spectrum (arb. units) vs Raman shift (cm^{-1}).

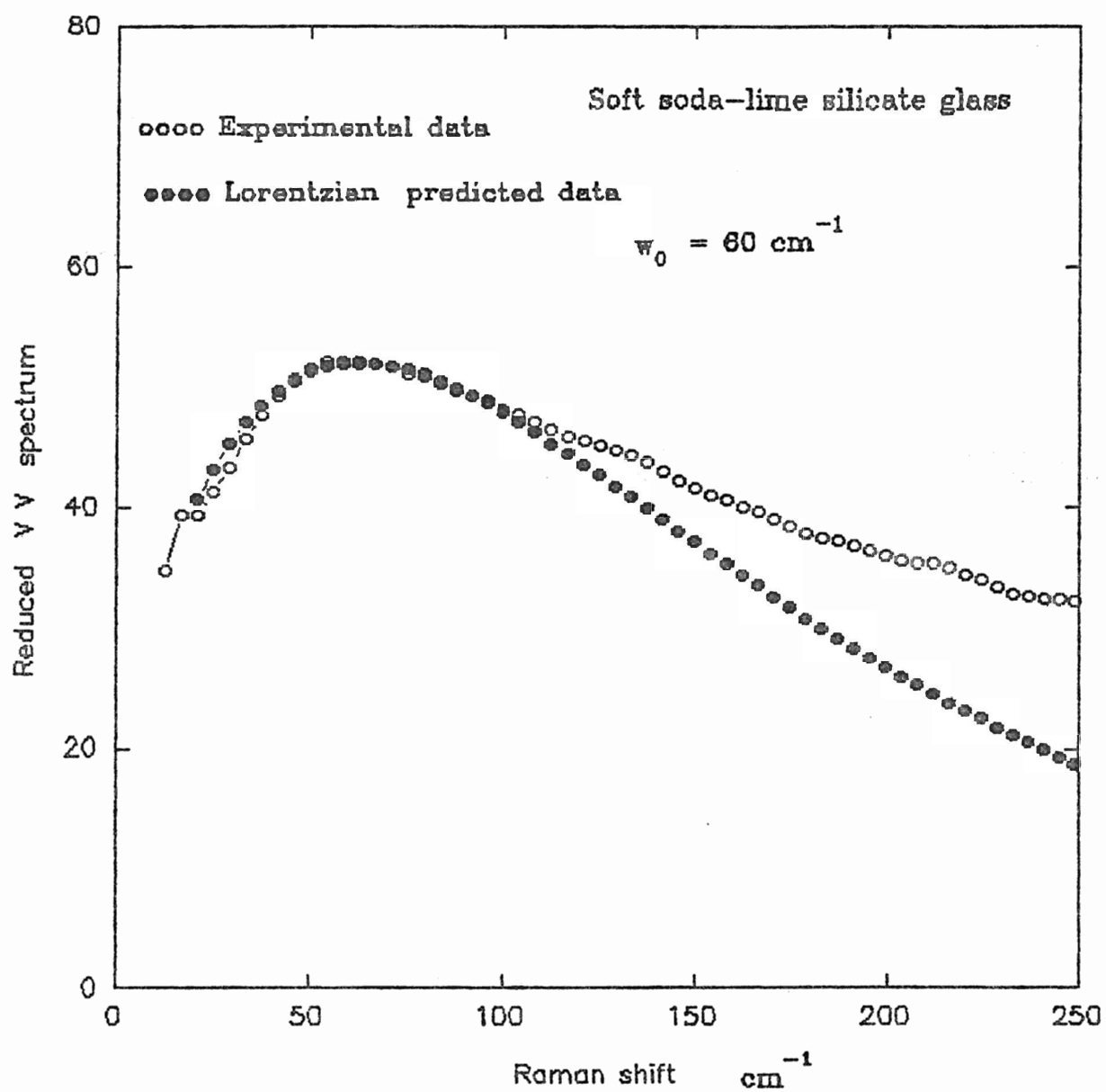
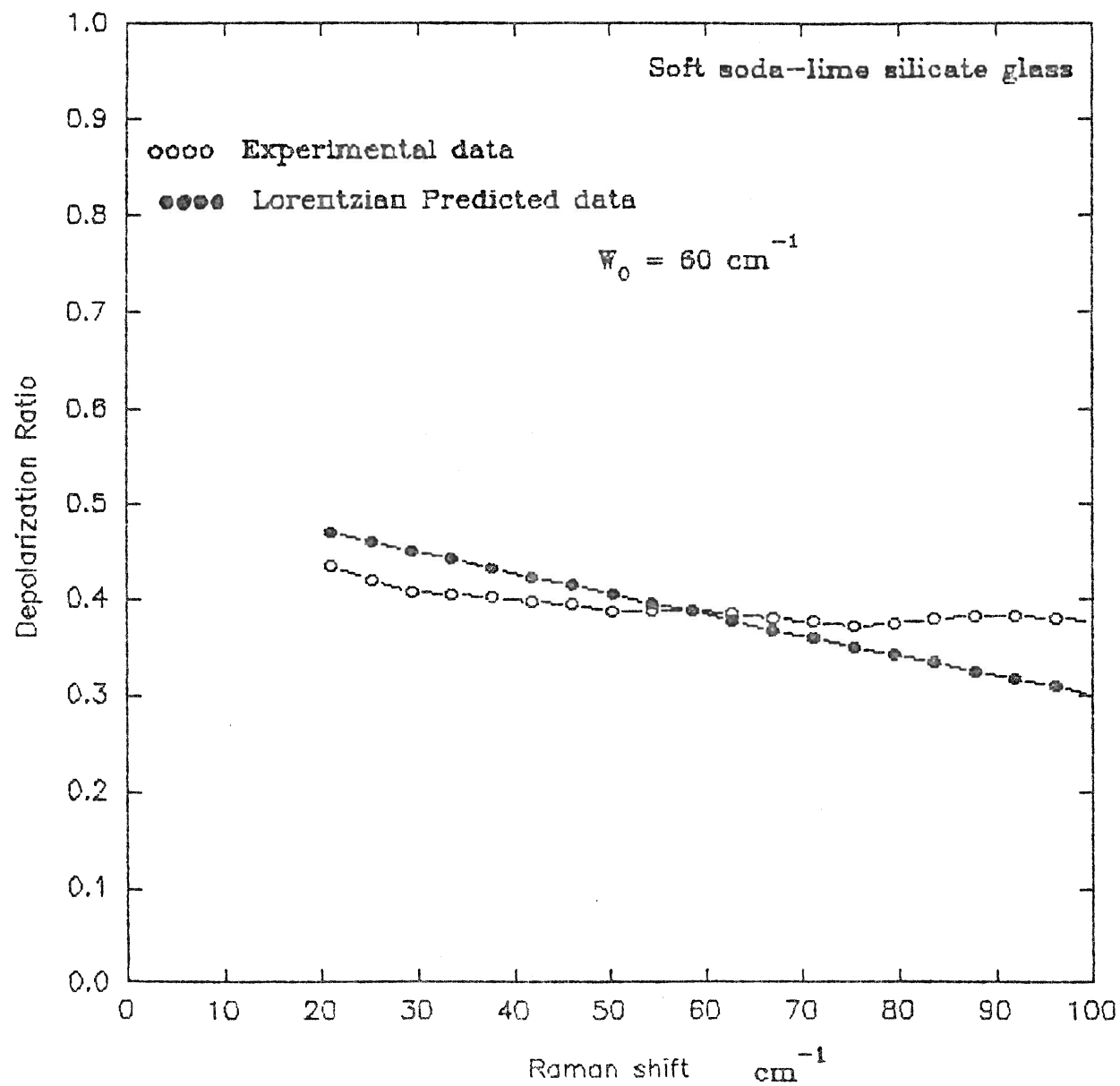


Fig. 4.35 Soft glass experimental and Lorentzian predicted depolarization ratio spectrum vs Raman shift (cm^{-1}).



5- DISCUSSION

The theoretical VV reduced spectra based on the MB model with Gaussian, Poisson, and Lorentzian forms of correlation function are given by Eqs (5), (11), and (13) respectively. The quantity M which appears in all these equations had to be selected in order to fit the theory to the experimental data. Since the frequency of the predicted maxima of the spectra are not very sensitive to M , it was chosen as the value which gave the best fit of the predicted depolarization to the experimental value at the peak of the LFB. For pyrex, the values of M required to fit the Gaussian, Poisson, and Lorentzian depolarization spectra to the experimental data at the maximum of the LFB were measured to be 0.30, 2.20, and 0.36 respectively. Figs 4.6, 4.9, and 4.12 indicate that the predicted spectrum based on a Poisson correlation function provided the best fit to the experimental data. The quantity M which is given by Eq (6), can be written as:

$$M = (C_L^2 / C_t^2) [\{ (\delta C_L^2 / C_L^2) + \lambda \} / \{ (\delta C_t^2 / C_t^2) + \lambda \}]$$

If the second term of the product is assumed to be 1 then;

$$M = (C_L / C_t)^2 \tag{17a}$$

$$\text{where } (C_L / C_t) = (1/3) (P_{11} + 2P_{12}) / (P_{11} - P_{12}) \tag{17b}$$

For pyrex, P_{11} and P_{12} are 0.1156 and 0.2370 respectively (Schroeder, 1980), so $M = 2.60$. This theoretically estimated M is in good agreement with the value of $M = 2.20$ obtained from fitting the Poisson predicted spectrum to the experimental values at the peak of the LFB. Therefore, the Poisson correlation function not only provides the best fit

but also gives the closest value of M to the theoretical estimate. The Gaussian and Lorentzian correlation functions required values of $M = 0.30$ and 0.36 respectively which are about one tenth of the theoretical estimate of M .

For quartz, the quantity M required to fit the Gaussian, Poisson, and Lorentzian depolarization spectra to the experimental data at the maximum of the LFB were measured to be 0.10 , 3.55 , and 0.64 respectively. Again using Eq (17), with the values of P_{11} and P_{12} for quartz as 0.1210 and 0.270 respectively (Schroeder, 1980), the estimated value of M is 2.19 . From Figs 4.17, 4.20, and 4.23 and a comparison of the values of M obtained from the Gaussian, Poisson, and Lorentzian correlation functions, it is concluded that again the Poisson correlation function provides the best fit to the experimental results.

For the soda-lime glass, the quantity M required to fit the Gaussian, Poisson, and Lorentzian depolarization spectra to the experimental values at the peak of the LFB were measured to be 0.85 , 7.0 , and 1.1 respectively. To our knowledge no measurements of P_{11} and P_{12} for the soda-lime silicate glass has been reported. However, Schroeder (1980) gives values for the photoelastic constants for compounds with similar composition to that of a soda-lime silicate glass. For compositions, such as $(\text{Al}_2\text{O}_3)_0 (\text{Na}_2\text{O})_{.25} (\text{SiO}_2)_{.75}$ and $(\text{Al}_2\text{O}_3)_{.5} (\text{Na}_2\text{O})_{.25} (\text{SiO}_2)_{.70}$, the values of (P_{11}, P_{12}) are $(0.1340, 0.2140)$ and $(0.1202, 0.2060)$ respectively. Again using Eq (17), the estimated values of M for these glasses are 5.48 and 4.27 respectively. From Figs 4.28, 4.31, and 4.34 it is clear that both the Poisson and Lorentzian correlation functions provide a good fit to the experimental results; however, from a comparison of the value of M

estimated for similar glasses it is again concluded that the Poisson correlation function gives the best fit to the experimental data.

The predicted VH reduced spectrum from any one of Eqs (4), (10), and (14) is dominated by the contribution of the first terms of the equation because the factor $(v_L / v_t)^5$ is ~ 15 for many glass materials (Heiman, Hamilton, and Hellwarth, 1979). Thus materials that are described by the same correlation function for the fluctuations of the photoelastic and elastic constants will have the same reduced VH spectrum when the frequency variable is replaced by ω/ω_0 . The dominant first term for the VH spectrum based on a Poisson correlation function is $(\omega^2 / (\omega^2 + \omega_0^2)^2)$. Malinovsky et al (1986) claimed that this term provides a universal fit to the experimental low-frequency VH spectrum for any glass regardless of its chemical composition.

Our experimental results for pyrex fitted to the reduced VH spectra based on the three different forms of the correlation function are shown in Figs. 4.5, 4.8, and 4.11. From Fig. 4.5, it is clear that the Gaussian function provides a good fit to the experimental data for $\omega \leq \omega_0$ (ω_0 is the peak of the LFB) but there is a strong deviation from the experimental results for $\omega > \omega_0$. The Poisson function as, shown in Fig. 4.8, provides a good fit in the entire region of interest. Fig. 4.11 shows that VH spectrum based on a Lorentzian function gives a poor fit for $\omega < \omega_0$ but the fit is good for $\omega \geq \omega_0$. Therefore, the Poisson correlation function predicts a VH spectrum which gives the best fit to the experimental data throughout the region of interest for pyrex.

For quartz, Fig. 4.16 shows that the VH Gaussian correlation function provides a good fit to the experimental data for $\omega \leq \omega_0$ but a sharp deviation from the experiment is observed for $\omega > \omega_0$. Fig. 4.19

shows that the Poisson VH provides a good fit to the experiment in the entire region of interest. Fig. 4.22 shows that the Lorentzian VH spectrum gives a good fit for $\omega \geq \omega_0$ but the fit is poor for $\omega < \omega_0$. Therefore, it is again concluded that the VH prediction by the Poisson form of correlation function provides the best fit to the experimental data in the entire region of interest.

Although for the soda-lime silicate glass the Lorentzian prediction of the VH spectrum seems to give the best fit to the experiment for the region of interest, we suspect the reliability of this specific experimental VH Stokes spectrum because of the shape of its lower wing. Unfortunately, due to a major equipment failure, the experiment could not be repeated. An anti-Stokes spectrum excited by the 488 nm line, which did not show the effects of the fluorescence, was used to predict the shape of the Stokes spectrum. The form of the Stokes spectrum excited by the 514.5 nm line was consistent with the predicted shape.

The fit of the depolarization ratios based on a Gaussian, Poisson, and Lorentzian correlation functions to the experimental values for pyrex are shown in Figs. 4.7, 4.10, and 4.13 respectively. For quartz, they are shown in Figs. 4.18, 4.21, and 4.24 and for the soda-lime silicate glass they are shown in Figs. 4.29, 4.32, and 4.35 respectively. In general all the Figs. show a reasonable fit to the theory for $\omega \geq \omega_0$; however, the predicted depolarization ratios fell significantly below the predicted values for $\omega < \omega_0$.

The uncertainties associated with the intensity measurements of the VV and VH spectra are magnified in the calculation of the experimental depolarization factor. However, these uncertainties are too small to produce the observed differences. The effects of partially polarized parasitic light at the laser frequency may affect the experimental depolarization factor at the lowest Raman frequencies (20 cm^{-1}) but should be negligible at frequencies near the peak of the LFB.

The expression for the VV intensity, or for the coupling constant C_{VV} , consists of two terms, one from the transverse modes and the other from the longitudinal term having its maximum at the higher frequency. The relative magnitudes depend on the value of the parameter M and the ratio of the acoustic wave speeds. Thus the maximum of the spectrum, experimental or reduced, should occur at a frequency determined by ω_0 , the frequency of the maximum of the LFB, the ratio v_L / v_t and the parameter M . It must occur at a frequency greater than ω_0 . For the materials of interest the difference is about 10 cm^{-1} . The maximum as calculated from the theory is broad and extends over 10 to

15 cm^{-1} with a variation in intensity of only 2%. Since our measurements of the spectra were made in channels of spectral width 4 cm^{-1} the distinction between the positions of the VV and VH peaks will be lost and each spectrum will appear to have its maximum at the same frequency. The maximum intensities of the VV and VH spectra were observed at the same frequency.

The broadening of the spectrum through the effects of the finite channel width will have an effect on the measured depolarization factor that would be greatest for those frequency regions in which the intensity is changing most rapidly, as is the case for the region between 20 and 40 cm^{-1} for each of the materials studied. However, the effect of the channel width should be the same for both VV and VH spectra and, therefore, should not be expected to produce great changes in the depolarization ratio. It may be noted that spectra of chalcogenide glasses (Nemanich, 1977) taken with spectral resolution of 1 cm^{-1} showed the expected difference in the positions of the VV and VH maxima but also gave a depolarization spectrum that showed a weak maximum at low frequency in contrast to the theoretical spectrum.

The values of the structural correlation radius, R_c or 2σ , and the parameter M , required to achieve the best fit of the three sets of equations for the coupling constants C_{VH} and C_{VV} to the reduced spectra, are set out in Table 1.

Table 1. Structural correlation radius R_c (nm) and the parameter M for pyrex boro-silicate glass, fused quartz, and soda-lime silicate glass for the three correlation functions: Gaussian, Poisson, and Lorentzian.

Correlation function	Pyrex boro-silicate glass		Fused quartz		Soda-lime silicate glass	
	$R_c(\text{nm})$	M	$R_c(\text{nm})$	M	$R_c(\text{nm})$	M
Gaussian	0.90	0.30	0.90	0.10	0.60	0.85
Poisson	0.83	2.20	0.80	3.55	0.52	7.00
Lorentzian	0.83	0.36	0.80	0.64	0.52	1.10

The results for the SCR for the quartz and the pyrex are similar. All three correlation functions set the radius at 0.80 - 0.90 nm. However, the values of the parameter M required to fit the results differ markedly from one function to another. The values of M obtained from the Gaussian and Lorentzian correlation functions are an order of magnitude below the value calculated from the values of the photoelastic constants for fused quartz and the pyrex glass. At the same time, these two functions provide a poor fit to the spectra below 100 cm^{-1} in contrast to the fit for the Poisson type of function.

The results for the soda-lime silicate glass required a value of the SCR, to get the best fit possible, between 0.50 and 0.60 nm for the three functions. Again there is a discrepancy between the values of M required by the different functions. Again the value of M required by the Poisson function is an order of magnitude greater than that required by the

others and it is closer to the estimated value for materials of similar composition (Schroeder, 1980) but significantly higher than for the quartz and pyrex glass. The soda-lime glass appears to show a shorter range correlation than the quartz or the pyrex glass by about 30%.

The difference in the results for the soda-lime glass on the one hand and the quartz and pyrex glass on the other is also present in the appearance of the spectra. Both quartz and pyrex glass exhibit similar spectra. For the VV case each has a clear maximum at $\sim 50 \text{ cm}^{-1}$ and $\sim 450 \text{ cm}^{-1}$ separated by a well-defined valley. For the VH case both show a single peak near 50 cm^{-1} that decays with increasing Raman frequency. The soda-lime glass VV spectrum has a maximum near 60 cm^{-1} and another near 600 cm^{-1} and separated by a shallow valley. The VH spectrum rises to a plateau that begins at $\sim 60 \text{ cm}^{-1}$ and continues to $\sim 900 \text{ cm}^{-1}$ in sharp contrast to the other materials. The same shape was obtained by calculating the Stokes spectrum from an anti-Stokes VH spectrum excited by the 488 nm line.

The MB theory for the frequency dependence of the coupling constants C_{VV} and C_{VH} is valid for a Debye vibrational density of states. But an upper limit was proposed for the application of the theory which has been taken to correspond to the frequency of the maximum reduced intensity of the VH spectrum. For the original Gaussian correlation function the strong departure of the theory from the experiment for frequencies above that of the maximum was taken as a demonstration of the limit (Nemanich, 1977, Lorosch et al, 1984). However, the introduction of the Poisson type correlation function (Malinovsky et al, 1986) in the theory has produced fits of the theory to experiment up to frequencies of twice

that maximum, as is confirmed in this work. It appears that the assumption of a Debye frequency spectrum is valid for the Raman scattering observed in the range from 20 - 100 cm^{-1} .

The structural correlation radius R_c is determined from the maximum of the VH reduced spectrum by Eq (9b) which also determines the frequency of the lowest toroidal mode of an isotropic elastic sphere whose surface is at rest. If the material in a sphere of radius R_c is identified as such a sphere the number of atoms in it for the quartz and the glasses is 300. Calculations of the vibrational modes of clusters of 500 atoms that simulate the structure of amorphous quartz have been made (Bell and Dean, 1968) but the results are not given for frequencies as low as 100 cm^{-1} .

Recent measurements of neutron scattering by low energy excitations of disordered materials (Dianoux, 1989) have shown that in amorphous quartz there is an excess density of states above the Debye spectrum that results in the observed maximum in the ratio specific heat $/T^3$ at 11 K. The density of the excess states has its maximum at 2 THz (67 cm^{-1}) and extends to 4 THz. Raman scattering attributed to these states has been reported (Winterling, 1975). The excess scattering over that expected for a Debye spectrum was measured for Raman frequencies up to 20 cm^{-1} at which point the excess vanished. There has been no evidence for an excess Raman scattering above 20 cm^{-1} . None has been found in this work.

6- Conclusion

Raman scattering for the amorphous materials fused quartz, "pyrex" boro-silicate glass and soft soda-lime silicate glass has been investigated for frequency region 20 to 100 cm^{-1} . The Raman experimental and reduced spectra for the VV and VH combinations of the polarization have been presented for each material. The shapes of the spectra and the depolarization ratios were compared with theoretical estimates based on the Martin and Brenig (MB) model with Poisson, Gaussian, and Lorentzian forms of the correlation function for the elastic and photoelastic constants. The structural correlation radius R_c , the parameter M , and the correlation function for the elastic and photoelastic constants were obtained from the fitting of the theory to the experimental VH and VV reduced spectra. The structural correlation radius for the quartz and the pyrex glass are similar. To achieve the best fit to the experimental data all three correlation functions required a value of SCR between 0.80 - 0.90 nm. The results for the soda-lime glass required a value of the SCR between 0.50 and 0.60 nm. The values of the parameter M and its theoretical estimate are listed in Table 2.

Table 2 The parameter M and its theoretical estimate for pyrex boro-silicate glass, fused quartz, and soda-lime silicate glass for the three correlation functions: Gaussian, Poisson, and Lorentzian.

Correlation function	Pyrex boro-silicate glass		Fused quartz		Soda-lime silicate glass	
	M	M_{exp}	M	M_{exp}	M	M_{exp}
Gaussian	2.60	0.30	2.19	0.10	5.48	0.85
Poisson	2.60	2.20	2.19	3.55	5.48	7.0
Lorentzian	2.60	0.36	2.19	0.64	5.48	1.10

The parameters M required to fit the experimental spectra to the theoretical values for the three correlation functions are markedly different. The value of M closest to the theoretical estimate was obtained for the Poisson correlation function in all cases.

The experimental VV spectra for quartz and pyrex glass were similar in shape and extent. The VH spectra were also similar in shape. For the soft glass the VV and VH spectra are markedly different from those of the quartz and pyrex glass. The features were less well defined than those of the quartz and pyrex glass and the extent VV of the spectrum was greater. The VH spectrum was plateau-like after 60 cm^{-1} in sharp contrast to the VH spectrum of the quartz and pyrex glass. The extent of the VH spectrum was also much greater than those of the quartz and pyrex glass. The depolarization ratios measured at the peak of the LFB for

quartz, pyrex glass, and soda-lime glass were 0.40, 0.53, and 0.38 respectively.

The best fits of the theoretical estimate to the experimental spectra were obtained by the MB model with a Poisson correlation function. Therefore, our results support the claim of Malinovsky and Sokolov (1986) that there is a universal fit to the shape of the LFB in the VH polarization for any glass regardless of its chemical composition.

Appendix I

The coupling constant for the scattering by phonons at Raman shift ω is proportional to the auto-correlation function of the fluctuations of the electrical susceptibility at frequency ω (Van Hove, 1954). For acoustic phonons in a continuous medium the components of the susceptibility fluctuations at \mathbf{R}_1 are related to the elastic strains $e_n(\omega, \mathbf{R}_1)$ by

$$\delta\chi_i = (\epsilon / 4\pi) p_{in}(\mathbf{R}_1) e_n(\omega, \mathbf{R}_1) \quad (\text{A.1})$$

where p_{in} is a photo-elastic or elasto-optical constant, for the material and ϵ is the dielectric constant. In an amorphous material $p_{in}(\mathbf{R}_1)$ can be written as an average value $\langle p_{in} \rangle$ plus a fluctuation part $p_{in}(\mathbf{R}_1)$. The average part only contributes to the Brillouin scattering at the zone centre and is of no interest for the LFB. The fluctuating part determines the LFB scattering.

For plane wave phonons of wave vector \mathbf{K} the elastic strains are

$$e_n(\omega, \mathbf{R}_1) = K e_n(\omega) \exp(i\mathbf{K} \cdot \mathbf{R}_1) \quad (\text{A.2})$$

and then the coupling constant is

$$C_b(\omega) = (\epsilon^2 / 4\pi)^2 K^2 e_n e_m^* \int d^3\mathbf{R} F(\mathbf{R}) \exp(i\mathbf{K} \cdot \mathbf{R}) \quad (\text{A.3})$$

where $F(\mathbf{R})$ is the correlation function of the fluctuations at \mathbf{R}_1 and \mathbf{R}_2 and $\mathbf{R} = \mathbf{R}_1 - \mathbf{R}_2$. The coupling constant is, therefore, the spatial Fourier transform of the fluctuations of the photoelastic constants appropriate to the polarization of the incident and scattered photons and the polarization

and wave vector of the phonons. The functions g_t and g_L that appear in Eq (2) of the MB theory are taken as the Fourier transform of the Gaussian correlation function by Nemanich (1977) and the transforms of the Poisson and Lorentzian correlation functions, Eq(9a) and Eq(12) respectively, by Malinovsky and Sokolov (1986).

REFERENCES

- T. W. Bril, Doctoral Thesis, Eindhoven (1976).
- R. J. Bell, N. F. Bird and P. dean J. Phys. **C1**, 299 (1986).
- A. J. Dianoux, Phil. Mag. (GB) **B59**, 17 (1989).
- P. Flubacher, A. J. Leadbetter, J. A. Morrison and B .P. Stoicheff,
J. Phys. Chem. Solids **12**, 53 (1959).
- D. Heiman, D. S. Hamilton and R. W. Hellwarth, Phys. Rev. **B19**,
6583 (1979).
- R. S. Krishnan, Proc. Ind. Acad. Sci. **A37**, 377 (1953).
- D. Krishnamurti, Proc. Ind. Acad. Sci. **A47**, 276 (1958).
- J. S. Lannin, Solid stats commun. **11**, 1523 (1972).
- J. S. Lannin, and P. J. Carroll, Phil. Mag. (GB) **B45**, 155 (1982).
- J. Lorosch, M. Couzi, J. Pelous, R. Macher and A. Levasseur,
J. Non-Cryst. Solids **69**, 1 (1984).
- V. K. Malinovsky and A. P. Sokolov, Solid state Commun. **57**,
757 (1986).
- V. K. Malinovsky and V. N. Novikov and A. P. Sokolov,
Physics Lett. **A123**, 19 (1987).
- A. J. Martin and W. Brenig, Phys. stat. Solidi **B64**, 163 (1974).
- R. J. Nemanich, Phys. Rev. **B16**, 1655 (1977).
- J. Schroeder, J. Non-Cryst. Solids **40**, 549 (1980).
- S. M. Shapiro, R. W. Gammon and H. Z. Cummins,
Appl. Phys. Lett. **9**, 157 (1966).

- R. Shuker and R. W. Gammon, Phys. Rev. Lett. 52, 222 (1970).R.
N. Sinclair and A. C. Wright, J Non-Cryst. Solids 57,
447 (1983).
- J. E. Smith, Jr., M. H. Brodsky, B. L. Crowder, M. I. Nathan and
A. Pinczuk, Phys. Rev. Lett. 62, 642 (1971).
- L. Van Hove, Phys. Rev. 95, 249 (1954).
- G. Winterling, Phys. Rev. B12, 2432 (1975).
- R. Zallen, "The Physics of Amorphous Solids", John Wiley and sons,
New York (1983).